Monthly Notices of the ROYAL ASTRONOMICAL SOCIETY

MNRAS **549,** 1–24 (2026)
Advance Access publication 2026 May 25

https://doi.org/10.1093/mnras/stag920

AT2024lhc and AT2024kmq in the landscape of featureless tidal disruption events

Yuhan Yao [1,2,3★] Ryan Chornock [2,3] Andrew Mummery,[4] Raffaella Margutti [2,3,5] Marat Gilfanov,[6,7] Muryel Guolo [8] Eric R. Coughlin [9] Wenbin Lu [3,5,10] Joheen Chakraborty [11] Dheeraj R. Pasham [12,13] Kate D. Alexander [14] Olivia Aspegren [2] Charlotte R. Angus [15] Xinze Guo [2,3,16] Xander J. Hall [17] Erica Hammerstein [2,3] K.-Ryan Hinds [18] Anna Y. Q. Ho [19] Xiaoshan Huang [20] Elias Kammoun [21] Natalie LeBaron [2,3] Matteo Lucchini [22] Zoë McGrath [18] Matt Nicholl [15] Daniel A. Perley [18] R. Michael Rich [23] Genevieve Schroeder [19] Xinyue Sheng [15] Jesper Sollerman [24] Jean Somalwar [2,3,25] Jacob L. Wise [18] Michael W. Coughlin [26] Andrew Drake [27] Matthew J. Graham [27] George Helou [28] Joahan C. Jaimes [21] Mansi M. Kasliwal [27] Ashish A. Mahabal [21,29] Pavel Medvedev [6] Josiah Purdum [30] Ben Rusholme [28] and Rashid Sunyaev[6,7]

Affiliations are listed at the end of the paper

Accepted 2026 May 11. Received 2026 May 4; in original form 2026 February 25

ABSTRACT

We study AT2024kmq and AT2024lhc, two tidal disruption events (TDEs) with blue featureless spectra associated with high-mass black holes ($M_{\rm BH} \sim 10^8\,{\rm M}_\odot$). Both events show optical precursors consistent with shock dissipation from stream self-intersection. Their X-ray emission is luminous ($L_{\rm X} \sim 10^{44}\,{\rm erg\,s^{-1}}$), highly variable (with minimum observed variability time-scales of 1.3 and 4.8 h for factor of ∼3 flux changes), long-lasting (>1 yr), emerging no later than the optical peak, and well characterized by power laws with $1.7 < \Gamma < 3$ (where $f_\nu \propto \nu^{1-\Gamma}$). The X-ray properties and radio non-detections support a compact corona ($\lesssim 10 r_{\rm g}$) producing Comptonized X-ray emission. Using all published featureless TDEs, we find statistically significant bimodality in the distribution of their peak ultraviolet/optical blackbody luminosities and radii. We assemble a comparison TDE sample with early-time X-ray observations with eROSITA, in which we find different $M_{\rm BH}$ distributions in TDEs with different X-ray spectral evolution properties: low-mass black holes ($M_{\rm BH} \sim 10^6{\rm M}_\odot$) remain soft ($\Gamma > 4$) within $t \lesssim 2$ yr, intermediate masses ($\sim 10^7{\rm M}_\odot$) transition from soft to hard at ∼1 yr, while high masses ($\sim 10^8{\rm M}_\odot$) are hard ($1.5 < \Gamma \lesssim 3$) from the outset. We interpret this result as evidence that the soft-to-hard state transition in TDEs occurs at the critical threshold of $\dot{M}_{\rm acc} \sim 0.03\dot{M}_{\rm Edd}$ (similar to X-ray binaries), using the fact that the transition time-scale predicted by simple disc theory scales with black hole mass as $t_{\rm tr} \propto M_{\rm BH}^{-3/4}$.

Key words: accretion – black hole physics – galaxies: nuclei – transients: tidal disruption events.

1 INTRODUCTION

Tidal disruption events (TDEs) occur when a star passes sufficiently close to a massive black hole (MBH) to be torn apart by tidal forces. The canonical tidal disruption radius

$$r_{\rm T} = R_\star (M_{\rm BH}/M_\star)^{1/3} = 3.2 \times 10^{13} M_{\rm BH,8}^{1/3} (\rho_\star/\rho_\odot)^{-1/3}\,{\rm cm}, \quad (1)$$

where $M_{\rm BH,8} \equiv M_{\rm BH}/(10^8\,{\rm M}_\odot)$; $R_\star$, $M_\star$, and $\rho_\star$ are radius, mass, and mean density of the star. First theoretically predicted in the 1970s (J. G. Hills 1975; J. H. Lacy, C. H. Townes & D. J. Hollenbach 1982), early observational candidates were identified in the soft X-ray (e.g. S. Komossa & N. Bade 1999), where emission originates from the inner accretion disc. In recent years, optical time-domain surveys have come to dominate TDE discoveries.

In TDEs, the mass fall-back rate is expected to follow a power-law decline $\dot{M}_{\rm fb} \propto t^{-5/3}$ (M. J. Rees 1988; E. S. Phinney 1989). Mass accretion on to the BH is delayed since it takes time for material to redistribute its angular momentum. Nevertheless, the mass accretion rate still varies by orders of magnitude over time-scales of years (see appendix A of A. Mummery et al. 2025b). This rapid evolution makes TDEs ideal testbeds for whether MBHs undergo accretion state transitions analogous to those observed in stellar-mass X-ray binaries (XRBs).

During the outbursts of transient BH XRBs, the systems transition between distinct spectral states as the accretion rate evolves.

★ E-mail: yuhanyao@berkeley.edu

At high accretion rates, systems are in the high soft state (HSS), where X-ray emission is dominated by thermal disc radiation. The inner disc radius is located at the innermost stable circular orbit (ISCO). At low accretion rates, they occupy the low hard state (LHS), characterized by power-law spectra from Comptonization in a hot corona with photon index $\Gamma \sim 1.5$–2.0 (R. A. Remillard & J. E. McClintock 2006; C. Done, M. Gierliński & A. Kubota 2007; M. Gilfanov 2010). Here, the inner disc is truncated at $r_{\rm tr} > 10^2 r_{\rm g}$, where the gravitational radius is

$$r_{\rm g} = \frac{GM_{\rm BH}}{c^2} = 1.5 \times 10^{13} M_{\rm BH,8}\,{\rm cm}. \quad (2)$$

Within $r_{\rm tr}$ there exists a hot accretion flow, and the exact value of $r_{\rm tr}$ likely depends on the mass accretion rate (F. Yuan & R. Narayan 2004, 2014). At sufficiently low rates, the thin disc is absent.

Between the HSS and the LHS lies the intermediate state (IMS), where the X-ray spectrum has comparable contributions from disc and power-law components and Γ softens to 2.0–2.5. The IMS is further divided into the hard intermediate state (HIMS) and soft intermediate state (SIMS). The HIMS $\rightarrow$ SIMS transition is associated with the optically thick, geometrically thin accretion disc extending inwards to replace the hot accretion flow (F. Yuan & R. Narayan 2014), and with crossing of the 'jet line' on the hardness–intensity diagram, where compact jet radio emission peaks during the HIMS and collapses in the SIMS (R. P. Fender, T. M. Belloni & E. Gallo 2004; T. M. Belloni 2010).

The transition between soft states (HSS and SIMS) and hard states (LHS and HIMS) is expected to occur around a critical dimensionless accretion rate (F. Yuan & R. Narayan 2014, equation 27)

$$\dot{m} \equiv \dot{M}_{\rm acc}/\dot{M}_{\rm Edd} \approx (0.06\text{-}0.08)\alpha, \quad (3)$$

where $\dot{M}_{\rm acc}$ is the accretion rate, $\dot{M}_{\rm Edd} \equiv L_{\rm Edd}/(0.1c^2)$, $L_{\rm Edd} = 1.26 \times 10^{38} (M_{\rm BH}/{\rm M}_\odot)\,{\rm erg\,s^{-1}}$ is the Eddington luminosity, and α is the 'viscous' nuisance parameter of N. I. Shakura & R. A. Sunyaev (1973). For typical values of $\alpha \sim 0.1$–0.4 (A. R. King, J. E. Pringle & M. Livio 2007), this yields $\dot{m} \sim 0.01$–0.03. Observations of BH XRBs are roughly consistent with this expectation: the soft-to-hard state transitions occur at $\sim$0.005–0.1 $L_{\rm Edd}$ with a mean of $0.03\,L_{\rm Edd}$ (T. J. Maccarone 2003; R. J. H. Dunn et al. 2010; B. E. Tetarenko et al. 2016; A. Vahdat Motlagh, E. Kalemci & T. J. Maccarone 2019).

Recent observations suggest that at least some TDEs exhibit state transitions (P. G. Jonker et al. 2020; T. Wevers et al. 2021; Y. Yao et al. 2022; M. Guolo et al. 2024; A. Hajela et al. 2025; V. Berger et al. 2026), but whether this phenomenon is universal across the TDE population, and how it depends on $M_{\rm BH}$ and $\dot{m}$, remain open questions.

In the optical band, TDEs exhibit distinctive observational signatures that distinguish them from other nuclear transients. Their peak optical luminosities span a range similar to supernovae (SNe), with $-17 \lesssim M_{\rm g,peak} \lesssim -23$ (Y. Yao et al. 2023). However, unlike SNe, TDEs maintain persistently hot temperatures: blackbody fits to UV/optical spectral energy distributions (SEDs) yield $T_{\rm bb} \sim$ few $\times\, 10^4$ K throughout their evolution (E. Hammerstein et al. 2023a), with minimal colour evolution. At late times (months to years post-peak), TDEs exhibit a characteristic UV/optical plateau phase that is consistent with a viscously spreading outer accretion disc (S. van Velzen et al. 2019; A. Mummery & S. A. Balbus 2020; A. Mummery et al. 2024; Y. Alush, N. C. Stone & S. van Velzen 2025; M. Guolo et al. 2025).

The optical spectra of many TDEs are characterized by broad emission lines of hydrogen, helium, and Bowen fluorescence features (see a thorough analysis of spectral evolution by P. Charalampopoulos et al. 2022). Using 17 TDEs selected from the first 1.5 yr of the Zwicky Transient Facility (ZTF; E. C. Bellm et al. 2019; M. J. Graham et al. 2019; R. Dekany et al. 2020) optical sky survey, S. van Velzen et al. (2021) proposed a spectroscopic classification scheme with three main classes: (i) TDE-H, exhibiting broad Hα and Hβ emission lines; (ii) TDE-H + He, showing broad Balmer lines plus a broad He II λ4686 complex, with most events also displaying Bowen fluorescence features (N III, O III); (iii) TDE-He, characterized by broad He II λ4686 emission only, with no broad Balmer lines.

E. Hammerstein et al. (2023a) expanded the sample to 30 TDEs from the first 2.5 yr of ZTF and identified a fourth class: (iv) TDE-featureless, characterized by a blue continuum with no discernible emission or absorption features. Additionally, earlier studies have associated a fraction of coronal line emitters with TDEs (e.g. S. Komossa et al. 2008; T.-G. Wang et al. 2011, 2012; F. Onori et al. 2022). This TDE-coronal spectroscopic class was also recovered through a retrospective search of TDEs in ZTF (Y. Yao et al. 2023).

The four TDE-featureless events presented in E. Hammerstein et al. (2023a) are all exceptionally luminous, with rest-frame g-band absolute magnitude $-23 \lesssim M_{g,\rm peak} \lesssim -20.5$, where intrinsic TDE rates are low (Y. Yao et al. 2023). Consequently, these events are typically discovered at high redshifts ($z > 0.1$). I. Andreoni et al. (2022) suggested this population might harbour off-axis jets, as the UV/optical properties of luminous featureless TDEs and jetted TDEs are similar (see also spectral analysis in E. Hammerstein et al. 2026). However, radio follow-up observations of a sample of eight overluminous TDEs (five of which are featureless) found no evidence of off-axis jets (Y. Yao et al. 2025). Recently, several subluminous featureless TDEs with $M_{g,\rm peak} \gtrsim -18$ have been identified (Y. Yao et al. 2022; J. Zhu et al. 2025), raising the question of whether the featureless class exhibits a continuous luminosity distribution or is intrinsically bimodal.

Understanding the population of luminous, spectroscopically featureless TDEs is of vital importance for several reasons. First, these events dominate the TDE population around high-mass BHs ($M_{\rm BH} \sim 10^8\,{\rm M}_\odot$), where $r_{\rm T}$ (equation 1) becomes comparable to $r_{\rm g}$ (equation 2). In this regime, general relativistic (GR) effects fundamentally shape the debris dynamics and energy dissipation. Luminous featureless TDEs therefore provide unique laboratories for testing shock and accretion physics in the strong-field limit. Second, at the high-mass end, measuring TDE rates as a function of BH mass constrains the event horizon suppression effect, which depends on both BH spin and stellar age (A. M. Beloborodov et al. 1992; M. Kesden 2012; D. J. D'Orazio, Loeb & Guillochon 2019; E. R. Coughlin & C. J. Nixon 2022; H.-T. Huang & W. Lu 2024). The observed rate decline at $M_{\rm BH} > 10^7\,{\rm M}_\odot$ thus probes the average spin of MBHs in quiescent galaxies (P. Du et al. 2022) – a quantity difficult to measure through other means. Finally, luminous TDEs will dominate samples at high redshift, where only the most energetic events remain detectable. Next-generation surveys, particularly the Vera C. Rubin Observatory's Legacy Survey of Space and Time (LSST; Ivezić et al. 2019) and the *Nancy Grace Roman Space Telescope*, will discover hundreds to thousands of such events at $z > 1$. However, the current sample remains small ($\sim$ 10 events), with limited multiwavelength characterization. Establishing a comprehensive

Table 1. Basic information for the two TDEs.

Parameter	AT2024kmq	AT2024lhc
ZTF name	ZTF24aapvieu	ZTF24aaoxmyb
t_0 (MJD)	60460.24495	60424.40988
z	0.192	0.2045
$E_{B-V,\mathrm{MW}}$ (mag)	0.0169	0.0233
$N_{\mathrm{H,MW}}$ (cm^{-2})	1.77×10^{20}	2.34×10^{20}
$\log(M_{\mathrm{gal}}/\mathrm{M}_\odot)$	$11.22^{+0.03}_{-0.04}$	$11.39^{+0.05}_{-0.06}$
$E_{\mathrm{B-V,host}}$ (mag)	$0.016^{+0.022}_{-0.011}$	$0.027^{+0.020}_{-0.016}$
σ_* ($\mathrm{km\,s}^{-1}$)	181 ± 21	230.5 ± 19.8
$\log(M_{\mathrm{BH}}/\mathrm{M}_\odot)^a$	8.30 ± 0.37	8.76 ± 0.34
$\log(M_{\mathrm{BH}}/\mathrm{M}_\odot)^b$	8.54 ± 0.37	8.81 ± 0.43
$\log(M_{\mathrm{BH}}/\mathrm{M}_\odot)^c$	$7.66^{+0.24}_{-0.20}$	$7.93^{+0.26}_{-0.24}$
0.2–2.3 keV L_{X} ($\mathrm{erg\,s}^{-1}$)	$< 1.6 \times 10^{42}$	$< 8.5 \times 10^{41}$
$L_{(\mathrm{O\,III})}$ ($\mathrm{erg\,s}^{-1}$)	$< 3.0 \times 10^{39}$	$< 5.2 \times 10^{39}$
$W1-W2$ (mag)	0.308 ± 0.020	0.307 ± 0.017

Note.[a] MBH mass estimated using the J. Kormendy & L. C. Ho (2013) M_{BH}–σ_* relation. [b] MBH mass estimated using the M_{gal}–M_{BH} scaling relation presented in Y. Yao et al. (2023). [c] MBH mass estimated using the TIDALSPIN package (A. Mummery 2024), treating the σ_*-based estimates as priors. See the text in Section 2.3.

understanding of their properties and rates is therefore essential to enable their use as probes of MBHs and stars at high redshifts.

In this work, we present comprehensive multiwavelength observations of two luminous featureless TDEs discovered by ZTF: AT2024kmq (ZTF24aapvieu) and AT2024lhc (ZTF24aaoxmyb). These events are particularly notable because they exhibit luminous hard X-ray emission contemporaneous with their optical peaks – a characteristic rarely observed in TDEs. We describe our discovery, classification, and basic properties in Section 2, followed by multiwavelength observations and analysis in Section 3. In Section 4, we discuss the likely origin of the X-ray emission and highlight challenges in explaining the UV/optical peak emission using currently available models. We conclude in Section 5. This work includes follow-up observations obtained through January 2026.

We adopt a standard flat Lambda cold dark matter (ΛCDM) cosmology with matter density $\Omega_{\mathrm{M}} = 0.3$ and the Hubble constant $H_0 = 70\,\mathrm{km\,s}^{-1}\,\mathrm{Mpc}^{-1}$. We use the notation $\mathcal{Q}_n \equiv \mathcal{Q}/10^n$ for quantities in CGS units, with the exception that $M_{\mathrm{BH},n} \equiv M_{\mathrm{BH}}/(10^n \mathrm{M}_\odot)$ for BH masses. All logarithms are base 10 unless otherwise stated. Uncertainties are reported at 68 per cent confidence (1σ), and upper limits at 3σ. We correct for Galactic extinction using the J. A. Cardelli, G. C. Clayton & J. S. Mathis (1989) extinction law with $R_V = 3.1$ and the E. F. Schlafly & D. P. Finkbeiner (2011) dust map.

2 DISCOVERY, CLASSIFICATION, AND BASIC INFORMATION

The discovery and identification of AT2024kmq as a TDE have been published by A. Y. Q. Ho et al. (2025), which presented follow-up observations obtained prior to October 2024. AT2024lhc was classified as a TDE by the ZTF group (Y. Yao et al. 2024a; R. Chornock 2024).

We use t_{obs} (t_{rest}) to denote the observer-frame (rest frame) time relative to t_0, which is time of the most recent ZTF upper limit prior to the first optical detection. The basic information for the two objects is presented in Table 1, including the optical reference epoch t_0, redshift z, Milky-Way extinction $E_{B-V,\mathrm{MW}}$, the Galactic hydrogen-equivalent column density $N_{\mathrm{H,MW}}$ (R. Willingale et al. 2013), the host galaxy total stellar mass M_{gal} and extinction $E_{B-V,\mathrm{host}}$ (see Section 2.1), the stellar velocity dispersion σ_* (see Section 2.2), the BH masses estimated using host-galaxy scaling relations, the upper limits of the host-galaxy X-ray and [O III] λ5007 narrow line luminosities (see Section 2.4), and the $W1-W2$ colour in the unWISE catalogue (Vega system; E. F. Schlafly, A. M. Meisner & G. M. Green 2019), where WISE stands for the Wide-field Infrared Survey Explorer.

2.1 Host stellar population synthesis

To estimate global host galaxy properties, we model the pre-flare archival ultraviolet–infrared (UV–IR) SED of the host galaxy using population synthesis via the PROSPECTOR software (B. D. Johnson et al. 2021) built on FSPS (C. Conroy, J. E. Gunn & M. White 2009), following the same data collecting and fitting procedures as adopted by S. van Velzen et al. (2021, Section 3). The galaxy stellar mass M_{gal} is derived from the surviving fraction of stars formed. The host galaxy extinction $E_{B-V,\mathrm{host}}$ is computed as $0.268 \times$ `dust2`, where `dust2` is the optical depth at 5500 Å of the D. Calzetti et al. (2000) attenuation curve.

2.2 Stellar velocity dispersion

For AT2024kmq, the central velocity dispersion was initially reported as $175 \pm 27\,\mathrm{km\,s}^{-1}$ from fitting the 4200–6800 Å Gemini Multi-object Spectrograph (GMOS) spectrum taken at $t_{\mathrm{rest}} = +8$ d[1] (A. Y. Q. Ho et al. 2025). However, we later identified flux calibration issues at the blue end. We therefore reextracted and refit the spectrum using the 5030–5600 Å region, obtaining $\sigma_* = 181 \pm 21\,\mathrm{km\,s}^{-1}$, which we adopt in this work.

For AT2024lhc, the host galaxy has been observed by the Sloan Digital Sky Survey (SDSS; J. E. Gunn et al. 2006) on 2003 June 1 ($t_{\mathrm{rest}} = -6337$ d) and by the Dark Energy Spectroscopic Instrument (DESI; DESI Collaboration 2026) on 2021 May 1 ($t_{\mathrm{rest}} = -904$ d). L. Simard et al. (2011) measured that the galaxy half-light radius is $r_{1/2} = 16.2$ kpc (4.8 arcsec), and the effective semi-major radius of the galaxy bulge is $r_{\mathrm{e}} = 20.7$ kpc (i.e. 6.2 arcsec). The SDSS (3 arcsec fiber size) pipeline measures $\sigma_* = 230.5 \pm 19.8\,\mathrm{km\,s}^{-1}$, and running the FASTSPECFIT software (J. Moustakas et al. 2023) on the DESI spectrum (1.5 arcsec fiber size; DESI Collaboration 2022) gives $\sigma_* = 270 \pm 26\,\mathrm{km\,s}^{-1}$. We adopt the SDSS value since its fiber size better matches $r_{1/2}$ and r_{e} where σ_* (in the M_{BH}–σ_* relationship) is defined.

2.3 Black hole masses

The J. Kormendy & L. C. Ho (2013) M_{BH}–σ_* relation gives $\log(M_{\mathrm{BH}}/\mathrm{M}_\odot)$ values of 8.30 ± 0.37 for AT2024kmq and 8.76 ± 0.34 for AT2024lhc. These estimates must be reconciled with the Hills mass constraint – the maximum BH mass capable of tidally disrupting a star before it is swallowed whole (J. G. Hills 1975).

For an observable TDE, the pericenter distance must exceed the innermost bound circular orbit radius, r_{IBCO}, which depends on the angle between the star's orbit with respect to the BH's

[1] At this epoch, the transient flux is $< 10\,\mu$Jy (> 21.4 mag, see Section 3.1.1), contributing negligible light to the spectrum.

spin axis ϕ, and the dimensionless spin parameter a (J. M. Bardeen, W. H. Press & S. A. Teukolsky 1972). For non-spinning BHs (i.e. $a = 0$) $r_{\rm IBCO} = 4r_{\rm g}$, and for prograde equatorial orbits with $a = 1$ we have $r_{\rm IBCO} = r_{\rm g}$. An analytic solution for the Hills mass accounting for spin effects is provided by A. Mummery (2024).

For solar-type stars, tidal disruption remains possible around $M_{\rm BH} \sim$ few $\times\, 10^8\,{\rm M}_\odot$BHs if they are rapidly spinning. However, disruption by a $M_{\rm BH} \sim 10^9\,{\rm M}_\odot$ BH, as suggested by the σ_*-based estimate for AT2024lhc, would typically require a more evolved, lower-density star. Treating the σ_*-based estimates as priors and incorporating the TDE identification as evidence, we use the TIDALSPIN[2] Bayesian framework (A. Mummery 2024) to infer revised black hole masses. This analysis yields $\log(M_{\rm BH}/{\rm M}_\odot) = 7.66^{+0.24}_{-0.20}$ and $|a_{\rm BH}| = 0.63^{+0.38}_{-0.20}$ for AT2024kmq, and $\log(M_{\rm BH}/{\rm M}_\odot) = 7.93^{+0.26}_{-0.24}$ and $|a_{\rm BH}| = 0.84^{+0.16}_{-0.15}$ for AT2024lhc.

In summary, while precise BH mass constraints remain challenging, both events are hosted by high-mass BHs with $M_{\rm BH} \sim 10^8\,M_\odot$.

2.4 Lack of X-ray/optical/IR AGN signatures

The host-galaxy X-ray luminosity upper limits (see Table 1) are constrained using archival observations from the eROSITA telescope (P. Predehl et al. 2021) onboard the *Spektrum-Roentgen-Gamma* (*SRG*) satellite (R. Sunyaev et al. 2021), obtained during 2020–2022.

In the GMOS spectrum of AT2024kmq and the SDSS/DESI spectra of AT2024lhc, we do not identify narrow emission lines typically observed in active galactic nuclei (AGNs). We place upper limits on their [O III] λ5007 line luminosities (see Table 1) by modelling the spectra using the PPXF software (M. Cappellari 2023), following the procedures adopted by Z. Zhang et al. (2026).

AGN can be broadly divided into radiative mode ($L/L_{\rm Edd} \gtrsim 0.01$) and jet mode ($L/L_{\rm Edd} \lesssim 0.01$). The general picture is that radiative-mode AGNs possess a geometrically thin, optically thick accretion disc with the inner disc radius at ISCO, whereas jet-mode AGNs are surrounded by an inner hot accretion flow and an outer truncated disc – similar to the soft and hard states in XRBs (T. M. Heckman & P. N. Best 2014).

For radiative-mode AGN, the [O III] λ5007 line luminosity correlates with the bolometric luminosity (T. M. Heckman & P. N. Best 2014). Using the bolometric correction of T. M. Heckman et al. (2004), we estimate the AGN bolometric luminosities to be $< 1.0 \times 10^{43}\,{\rm erg\,s^{-1}}$ and $< 1.8 \times 10^{43}\,{\rm erg\,s^{-1}}$ for AT2024kmq and AT2024lhc, respectively. These upper limits rule out the existence of radiative-mode AGNs in their host galaxies, consistent with the fact that their mid-infrared (MIR) $W1 - W2$ colours are not AGN-like (D. Stern et al. 2012).

While the host galaxies may harbour jet-mode AGNs (discussed in Section 3.5), the absence of radiative-mode AGNs indicates there is no pre-existing disc extending to the ISCO. Therefore, the luminous optical transients cannot be caused by sudden changes in the mass accretion rate of a pre-existing AGN disc.

[2]The input data to TIDALSPIN is the black hole mass and its uncertainty given by the J. Kormendy & L. C. Ho (2013) $M_{\rm BH}$–σ_* relation. We note that this package assumes a stellar mass function in the form of the Kroupa initial mass function (P. Kroupa 2001), which might not be accurate in the nuclei of TDE host galaxies.

3 OBSERVATIONS AND ANALYSIS

3.1 Optical photometry

3.1.1 ZTF and ATLAS

We obtained ZTF (F. J. Masci et al. 2019, 2023) and Asteroid Terrestrial-impact Last Alert System (ATLAS; J. L. Tonry et al. 2018; K. W. Smith et al. 2020; L. Shingles et al. 2021) forced photometry. For ATLAS data, we cleaned and corrected the photometry using the `ATClean` method (S. Rest et al. 2025). Baseline correction was performed using the methods outlined in Y. Yao et al. (2019).

The Galactic extinction-corrected optical light curves of AT2024lhc and AT2024kmq are shown in the upper panels of Figs 1 and 2, respectively. They exhibit significant optical precursors at $t_{\rm rest} < 10$ d. The precursor in AT2024kmq is particularly prominent: it was initially identified as an independent fast-evolving transient before the main TDE flare emerged. Fig. 3 highlights these precursor light curves in flux space. We discuss their physical interpretation in Section 4.3.

3.1.2 LT

We obtained follow-up photometry of both events using the IO:O Optical Imager on the Liverpool Telescope (LT; I. A. Steele et al. 2004). Image subtraction was performed using reference images from Pan-STARRS1 (PS1; K. C. Chambers et al. 2016) for the *g*, *r*, *i*, and *z* bands, and from SDSS (F. D. Albareti et al. 2017) for the *u* band.

For AT2024lhc, we performed aperture photometry on the LT data using the 'Photometry Sans Frustration' routine described in M. Nicholl et al. (2023), which uses an optimal aperture that captures 90 per cent of point spread function flux after template subtraction. For AT2024kmq, photometry was obtained following the point spread function modelling technique described in C. Fremling et al. (2016).

In addition, for AT2024kmq we include LT and Lowell Discovery Telescope (LDT) photometry published by A. Y. Q. Ho et al. (2025). The LT and LDT photometry are shown in Figs 1–2. Both instruments employ SDSS filters.

The LT *z* band data were not included for further analysis, as we found that photometric uncertainties are underestimated in this band.

3.2 Optical spectroscopy

We obtained low-resolution optical spectra using the Kast spectrograph on the Shane 3-m telescope at Lick Observatory (J. S. Miller & R. P. S. Stone 1993), the Low Resolution Imaging Spectrograph (LRIS; J. B. Oke et al. 1995) on the Keck-I telescope, and the Alhambra Faint Object Spectrograph and Camera (ALFOSC[3]) at the 2.56 m Nordic Optical Telescope (NOT) located at the Roque de los Muchachos Observatory on La Palma (Spain). These observations were coordinated using the *fritz.science* instance of SKYPORTAL (S. van der Walt, A. Crellin-Quick & J. Bloom 2019;

[3]http://www.not.iac.es/instruments/alfosc

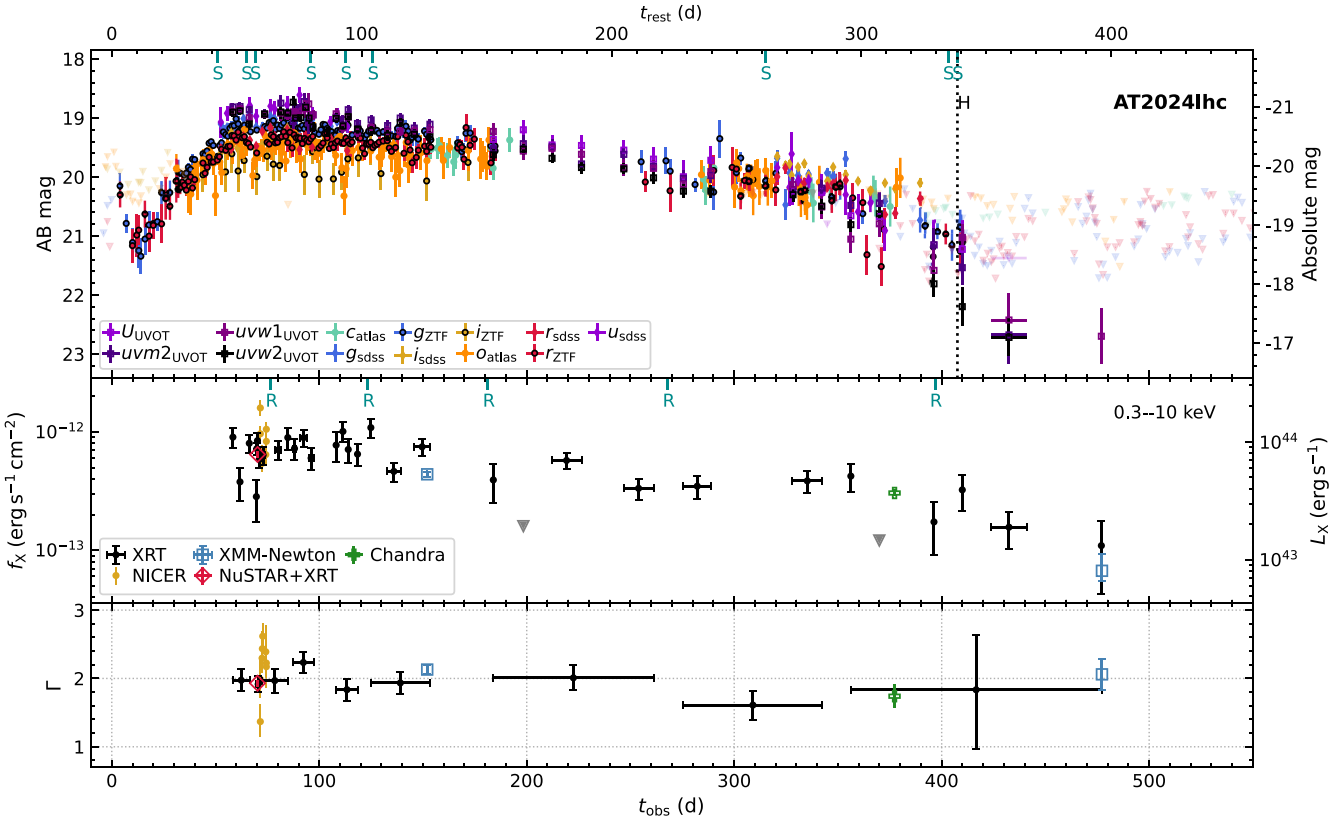

Figure 1. UV, optical, and X-ray evolution of AT2024lhc. UV and optical light curves are shown in the upper panel, with epochs of optical spectroscopy marked with letter 'S', and the epoch of *HST* spectroscopy marked with a vertical dotted line. Solid points represent detections above 3σ in the optical and above 2σ in the UV; semitransparent downward triangles indicate 3σ upper limits. The observed 0.3–10 keV X-ray light curves are shown in the middle panel, with epochs of radio continuum observations marked with letter 'R'. The evolution of the X-ray power-law photon index Γ is shown in the lower panel.

M. W. Coughlin et al. 2023). The observing log is provided in Table B1. Epochs of spectroscopic observations are marked with 'S' in Figs 1–2.

Kast observations were obtained with the D57 dichroic, 600/4310 grism (blue), and 300/7500 grating (red), unless otherwise noted in Table B1. Reductions followed J. M. Silverman et al. (2012). LRIS observations used the 600/4000 grism (blue), D56 dichroic, and 400/8500 grating (red). ALFOSC observations employed grism 4 and were reduced using a custom PYPEIT fork (J. X. Prochaska et al. 2020a; J. X. Prochaska et al. 2020b).

3.2.1 *AT2024kmq*

Fig. 4 shows optical spectra of AT2024kmq obtained after October 2024; earlier spectra are presented in A. Y. Q. Ho et al. (2025). No prominent broad emission lines characteristic of TDEs are detected at any epoch, confirming the spectroscopically featureless nature reported by A. Y. Q. Ho et al. (2025) at earlier times. We do not perform host-transient decomposition due to the lack of a pre- or post-flare host spectrum template.

3.2.2 *AT2024lhc*

Fig. 5 shows optical spectra of AT2024lhc. To search for transient spectral features, we model each spectrum as the sum of host galaxy and blackbody continuum contributions. The +335 d LRIS spectrum serves as the host template: at this epoch, the transient had faded to $g = 21.2$ mag and contributed negligibly to the observed flux.

Fig. 6 shows the host–blackbody decomposition. At all epochs, the combination of host and blackbody reproduces the observed spectra with no significant residual features. We therefore classify AT2024lhc as spectroscopically featureless throughout the observed evolution from $t_{rest} = +42$ d to +262 d, with no detection of the broad H, He, or Bowen emission lines characteristic of other optically selected TDEs.

3.3 *Swift*/UVOT

Both AT2024lhc and AT2024kmq were observed by the Ultra-Violet/Optical Telescope (UVOT; P. W. A. Roming et al. 2005) onboard *Swift*. We obtain the host-subtracted UVOT fluxes using the same procedures as outlined in A. Y. Q. Ho et al. (2025). Due to the lower signal-to-noise ratio (S/N) at late times, some of the adjacent observations are stacked using the same procedures as in Y. Yao et al. (2024b).

3.4 X-ray observations

We obtained X-ray observations with the X-Ray Telescope (XRT; D. N. Burrows et al. 2005) on board *Swift*, the Neutron Star Interior Composition Explorer (NICER; K. C. Gendreau et al. 2016), the Nuclear Spectroscopic Telescope ARray (NuSTAR; F. A. Har-

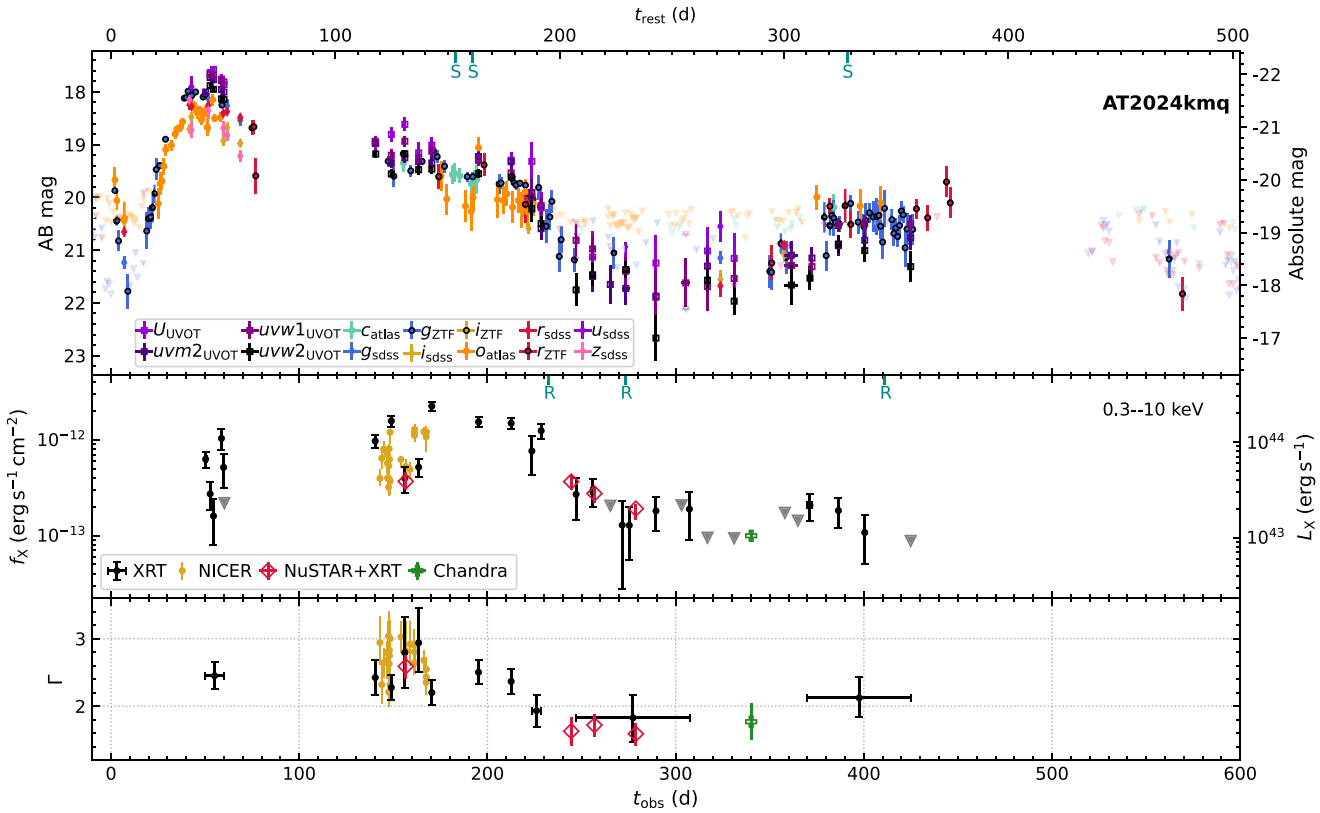

Figure 2. UV, optical, and X-ray evolution of AT2024kmq. We only indicate epochs of optical spectroscopy and radio observations first presented in this work, see A. Y. Q. Ho et al. (2025) for earlier observations.

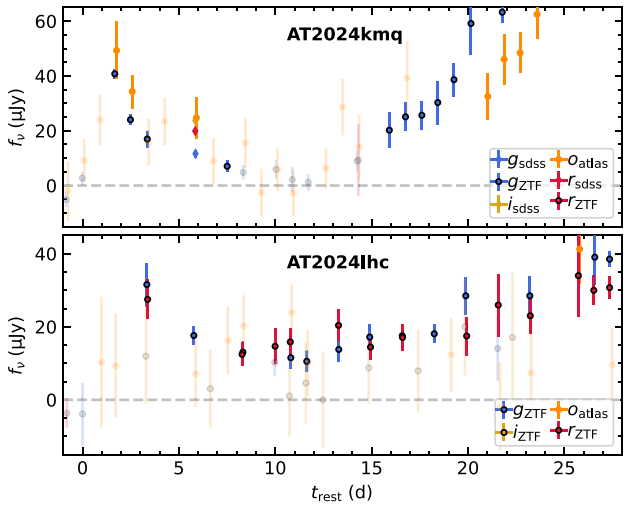

Figure 3. Early-phase optical light curves of AT2024kmq and AT2024lhc in flux space, showing the precursor emission detected in both events. Solid and semitransparent points represent $> 3\sigma$ detections and other observations, respectively. The dashed horizontal line at zero is the average value pre-transient.

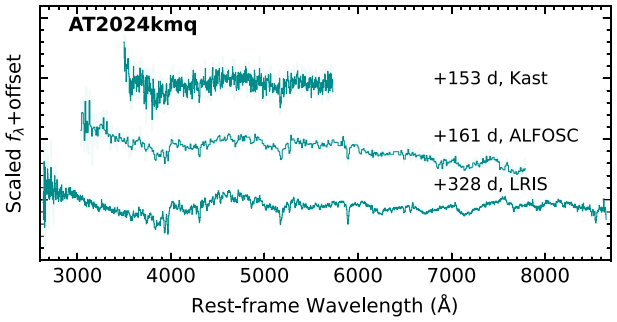

Figure 4. Optical spectra of AT2024kmq obtained after October 2024 (see A. Y. Q. Ho et al. 2025 for earlier epochs). Strong telluric features in the ALFOSC spectrum are masked. No prominent broad emission lines characteristic of TDEs are detected.

rison et al. 2013), the *Chandra* X-ray Observatory (CXO), and the *XMM–Newton* telescope.

The *Swift*/XRT, NICER, and NuSTAR data presented here are processed using HEASOFT version 6.34. The *XMM–Newton* data are reduced with the *XMM–Newton* Science Analysis System (SAS; C. Gabriel et al. 2004). The *Chandra* data are reduced using the *Chandra* Interactive Analysis of Observations (CIAO; A. Fruscione et al. 2006) software package (v4.17).

3.4.1 *Swift*/XRT

We processed *Swift*/XRT data following standard procedures outlined in A. Y. Q. Ho et al. (2025). To improve the signal-to-noise ratio (SNR) of XRT spectra at late times, we stacked consecutive observations. Spectra were binned using the optimal scheme of J. S. Kaastra & J. A. M. Bleeker (2016) (minimum one count per bin via `ftgrouppha`) and modelled with W-statistics (W. Cash 1979)

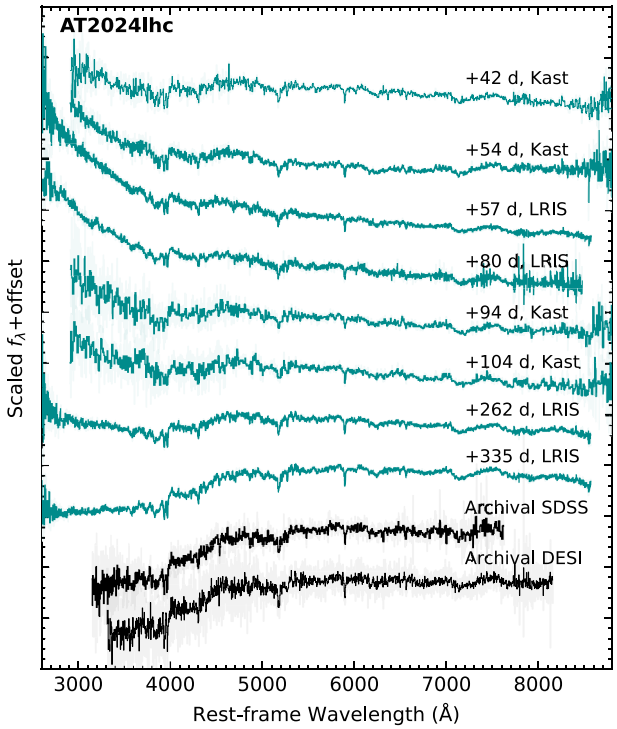

Figure 5. Optical spectroscopic observations of AT2024lhc. All epochs remain spectroscopically featureless (see Fig. 6).

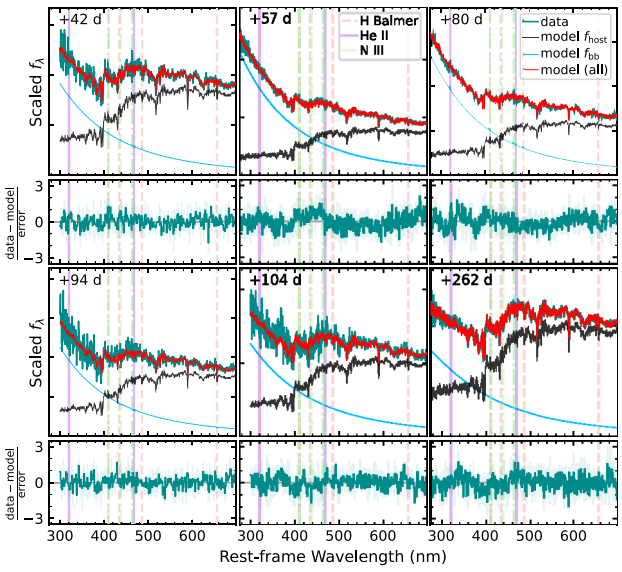

Figure 6. Host-transient decomposition for the optical spectra of AT2024lhc. Galactic extinction-corrected spectra are modelled as the sum of host galaxy emission and blackbody continuum. Residuals show no significant broad features, confirming AT2024lhc as spectroscopically featureless from $t_{\rm rest} = 42$ d to 262 d.

using an absorbed power law (`tbabs*zashift*powerlaw` in XSPEC), where $N_{\rm H}$ is fixed at the Galactic value given in Table 1. This simple model provides adequate fits to all spectra. From each best-fitting model, we derived the 0.3–10 keV count-rate-to-flux conversion factor, which was used to convert X-ray count rates (or their upper limits) from individual (unstacked) XRT snapshot observations into fluxes. Figs 1–2 (middle and bottom panels) show the evolution of the observed-frame 0.3–10 keV flux ($f_{\rm X}$) and power-law photon index Γ.

3.4.2 *NICER*

AT2024lhc was observed by the NICER X-ray Timing Instrument in July 2024 (obsID 7204630101–7204630108) for a total of 13.4 ks (PI: Yao). AT2024kmq was observed by NICER in October–November 2024 (obsID 7204930101–7641010107) and February–March 2025 (obsID 7641010107–7641010119, 7716010101–7716010129; PIs: Guolo, Pasham). For AT2024kmq, an offset of ∼0.7 arcsec was applied to NICER pointing to minimize contamination from a nearby X-ray source.

As both sources are faint and hard, we followed the time-resolved spectroscopy approach for reliable estimation of faint-source light curves outlined in section 2.1 of J. Chakraborty et al. (2024), which we summarize here. We divided the data into continuous good-time intervals (GTIs) determined by the NIMAKETIME routine. We then fit the spectrum of each GTI with the SCORPEON [4] model over a broad-band energy range (0.25–10 keV) for data taken in orbit night, and a slightly restricted range (0.38–10 keV) during orbit day. SCORPEON is a semi-empirical, physically motivated background model which explicitly includes components for the cosmic X-ray background, fluorescence emission from the solar wind charge exchange, and non-X-ray noise events (e.g. precipitating electrons and cosmic rays), allowing these to be fit alongside the source for joint uncertainty estimation. We grouped our spectra with the optimal binning scheme of J. S. Kaastra & J. A. M. Bleeker (2016), i.e. `grouptype = optmin` with `groupscale = 10` in the `ftgrouppha` command, and performed all spectral fitting with the Cash statistic. We used a ΔC-stat threshold of 25 to claim a source detection, and retained only GTIs with a best-fitting C-stat/d.o.f ≤ 1.5. The evolution of $f_{\rm X}$ and Γ are shown in Figs 1–2.

3.4.3 *NuSTAR*

We obtained NuSTAR observations for both events under pre-approved Target of Opportunity (ToO) programmes, summarized in Table B2.

To generate the source NuSTAR spectra for the two photon counting detector modules (FPMA and FPMB), source photons were extracted from a circular region with a radius of $r_{\rm src} = 35$ arcsec centred on the optical position of the source. The background was extracted from a $r_{\rm bkg} = 80$ arcsec region located on the same detector. We selected energy ranges where the net count rate is above the background for spectral fitting. The best-fitting absorbed power-law models, shown in Fig. A1, provide adequate description to the data. The best-fitting values of Γ and $f_{\rm X}$ are given in Table B2, and plotted in Figs 1–2.

3.4.4 *XMM–Newton*

AT2024lhc was observed with *XMM–Newton* at two epochs. We processed the observation data files (ODFs) following the procedures outlined in M. Guolo et al. (2024). Our analysis focuses

[4] https://heasarc.gsfc.nasa.gov/docs/nicer/analysis_threads/scorpeon-overview

Table 2. Rest-frame X-ray variability time-scales.

Name	Instrument	Phase $t_{\rm rest}$ (d)	$t_{\rm X,var}$ (d)	Significance (σ)	Flux ratio
		124.0	0.108	3.7	2.1
AT2024kmq	NICER	124.4	0.053	4.0	3.2
		134.2	1.840	4.8	2.4
AT2024lhc	XRT	57.4	0.199	3.1	2.6

on EPIC-pn data, which offers a higher SNR than the MOS detectors.

We group the spectrum using the J. S. Kaastra & J. A. M. Bleeker (2016) scheme and simultaneously ensure at least 10 counts per bin. Using W-statistics, we fit in the energy range where the source dominates, which is 0.3–2.9 keV for the first epoch and 0.3–2.5 keV for the second epoch. The fitting result is shown in Table B3 and Fig. 1.

3.4.5 *Chandra*

For both events, we obtain one epoch of observation with the CXO. We used the Advanced CCD Imaging Spectrometer (ACIS; G. P. Garmire et al. 2003), with the aim point on the back illuminated S3 chip. Both objects are clearly detected. We extract the source spectrum using a source region of $r_{\rm src} = 2.0$ arcsec centred on the apparent X-ray position of each object. A total of 65 and 193 (0.5–8 keV) counts are detected within the source regions of AT2024kmq and AT2024lhc, respectively. The background spectra are extracted using nearby source-free regions. We group the *Chandra* spectra to at least one count per bin, and modelled the 0.3–8 keV data using W-statistics. Using `tbabs*zashift*powerlaw`, we obtained good fits with best-fitting parameters shown in Table B3 and Figs 1–2.

3.4.6 *X-ray variability time-scale*

Both AT2024kmq and AT2024lhc exhibit significant X-ray variability on short time-scales. To quantify this, we systematically test all observation pairs separated by less than 2 d (observer frame) for statistically significant flux changes. For a pair to be classified as variable, we require both (1) a significance level exceeding 3σ and (2) a flux ratio exceeding a factor of 2.

For NICER observations (flux-calibrated measurements from Section 3.4.2), we compute the significance of flux variations as $\sigma = |F_2 - F_1|/\sqrt{\sigma_{F_1}^2 + \sigma_{F_2}^2}$, where F_1 and F_2 are the fluxes in two consecutive observations with uncertainties σ_{F_1} and σ_{F_2}. For *Swift* XRT observations (net count rate measurements from Section 3.4.1), we similarly compute the significance of net count rate variations. The flux ratio is defined as $\max(F_2/F_1, F1/F2)$ (or equivalently for count rates).

NICER detected rapid variability in AT2024kmq, with three significant events at rest-frame phases $t_{\rm rest} \sim 124$–134 d (Table 2). The minimum detected variability time-scale is $\Delta t_{\rm rest} = 0.053$ d ≈ 1.3 h, with a flux ratio of 3.2 and significance of 4.0σ. *Swift*/XRT detected one significant variation in AT2024lhc at $t_{\rm rest} = 57.4$ d, with $\Delta t_{\rm rest} = 0.199$ d ≈ 4.8 h (flux ratio 2.6, 3.1σ).

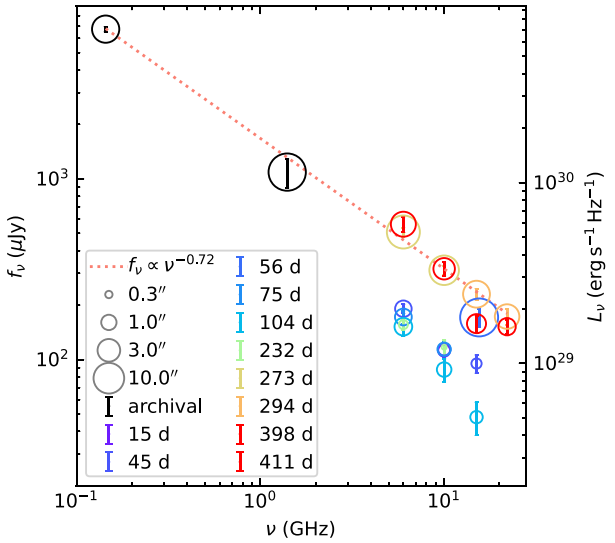

Figure 7. The SED of a radio source at the nucleus of AT2024kmq's host galaxy, colour-coded by $t_{\rm obs}$ (shown in the legend). Data at $t_{\rm obs} > 200$ d are presented in this paper (the integrated flux in Table B5), and are compared to earlier data presented in A. Y. Q. Ho et al. (2025). Symbol size reflects the synthesized beam size (full width at half-power) at each frequency. Observations with larger beams resolve extended emission from the pre-existing radio source, yielding higher integrated flux densities than measurements at higher resolution.

3.5 Radio: Very Large Array (VLA)

We obtained radio observations using the Very Large Array (VLA; R. A. Perley et al. 2011) under Programs 24A-487, 24A-494, and 25A-152 (PI: Y. Yao). The data were analysed following the standard radio continuum image analysis procedures in the Common Astronomy Software Applications (CASA; CASA Team 2022). We used TCLEAN to produce radio images.

For AT2024lhc, we measured the flux density as the maximum pixel value within a region with the size of the synthesized beam, centred on the optical coordinate of the TDE. The uncertainty was estimated as the root-mean-square (rms) of the pixel values in a nearby source-free region of the image. AT2024lhc was not detected throughout the observations, and 3σ upper limits are reported in Table B4.

For AT2024kmq, A. Y. Q. Ho et al. (2025) reported that the host is a radio-bright AGN with extended radio emission. Therefore, we used the interactive two-dimensional fit tool in CASA viewer, which fits Gaussians to two-dimensional intensity distributions. The measured peak and integrated fluxes are reported in Table B5. The integrated flux can be directly compared with earlier measurements reported in A. Y. Q. Ho et al. (2025). Fig. 7 shows the radio flux measurements from both A. Y. Q. Ho et al. (2025) and this work. Fitting observations obtained using large beam sizes (>3 arcsec), we obtained $f_\nu \propto \nu^{-0.72}$, which is typical for

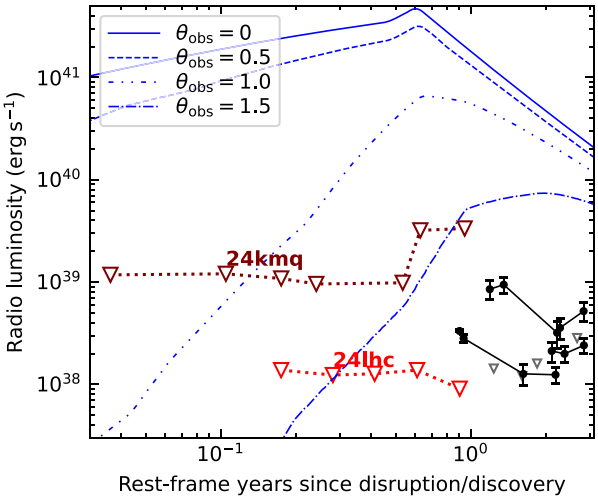

Figure 8. Radio upper limits of AT2024kmq, AT2024lhc, compared with the sample of optically overluminous TDEs presented in Y. Yao et al. (2025). The blue lines show model radio light curves for a jet with the same intrinsic properties as the best-fitting model of the jetted TDE *Swift* J1644+57 (P. Beniamini, T. Piran & T. Matsumoto 2023), viewed at different angles. Assuming all other parameters are identical, even the most off-axis jet models are ruled out for both AT2024kmq and AT2024lhc.

radio AGNs (J. J. Condon, W. D. Cotton & J. J. Broderick 2002). Due to the presence of the AGN, we are not able to set strong constraints on the radio emission of the TDE. Following A. Y. Q. Ho et al. (2025), we assume that the transient flux is lower than the measured flux densities.

3.5.1 *Constraints on transients: no J1644-like jets*

Fig. 8 presents the radio upper limits of AT2024kmq and AT2024lhc with other optically overluminous TDEs selected by ZTF (Y. Yao et al. 2025). These limits rule out off-axis jets with properties that are the same as those observed in the jetted TDE *Swift* J1644+57 (see figure caption for details).

3.5.2 *Constraints on host galaxies*

As discussed in A. Y. Q. Ho et al. (2025), the pre-TDE radio spectral index and luminosity of AT2024kmq are consistent with jet-mode AGNs. Its 1.4 GHz luminosity ($L_{1.4\,\mathrm{GHz}} = 4.6 \times 10^{23}\,\mathrm{W\,Hz^{-1}}$) indicates a jet mechanical power of $P_{\mathrm{mech}} = 3.5 \times 10^{36}$ W, using the P_{mech}–$L_{1.4\,\mathrm{GHz}}$ relation by T. M. Heckman & P. N. Best (2014, equation 2). The Eddington-scaled accretion rate is therefore $\dot{m} \approx L_{\mathrm{mech}}/L_{\mathrm{Edd}} \sim 0.003$. At such an accretion rate, the inner disc radius is likely $r_{\mathrm{tr}} \sim$ few $\times\, 10 r_{\mathrm{g}} \sim 10^{15}$ cm.

3.6 Blackbody modelling

Following previous TDE studies, we model the UV and optical photometry using a Planck function, where the SED is characterized by an effective temperature T_{bb} and a photospheric radius R_{bb}. We assume negligible host extinction based on two facts: (1) host galaxy population synthesis modelling yields very small reddening values (see Table 1), and (2) the X-ray spectra can be well fit by a simple power law absorbed by Galactic interstellar medium (ISM), with no need to add absorption from extragalactic ISM (see Section 3.4).

At epochs where both UV and optical photometry are available, we perform the fit using Monte Carlo Markov chain (MCMC) simulations with EMCEE (D. Foreman-Mackey et al. 2013). Both detections and non-detections are incorporated in the fitting following the procedures outlined in T. Laskar et al. (2014) and T. Eftekhari et al. (2024). We allow both T_{bb} and R_{bb} to vary freely. To account for systematic uncertainties in the photometry and potential deviations of the true SED from a pure blackbody, we use a Gaussian likelihood function that includes an excess variance term σ_0^2 that is constant across all bands. We set the priors to be uniformly distributed in the following ranges: $\log(T_{\mathrm{bb}}/\mathrm{K})$ in [3.2, 5.1], $\log(R_{\mathrm{bb}}/\mathrm{cm})$ in [12, 16.5], and $\log\sigma_0$ in $[-6, -0.5]$. Within the ensemble, we use 100 walkers, each of which is run until convergence, where the convergence test follows the steps outlined in Y. Yao et al. (2019).

At epochs with only optical data, we fix T_{bb} to the linearly interpolated value derived from epochs with UV coverage. We estimate R_{bb} directly from the radio of νL_ν and the colour correction for blackbody spectrum.

The results are shown in Fig. 9. AT2024kmq and AT2024lhc exhibit several notable similarities:

(i) Both events show precursor emission lasting ~ 8 d above survey sensitivity and peaking at $10^{43.5}$–10^{44} erg s^{-1}, though with different thermal properties: AT2024lhc has $T_{\mathrm{bb}} \sim 2 \times 10^4$ K and $R_{\mathrm{bb}} \sim 10^{15}$ cm, while AT2024kmq exhibits a lower temperature ($T_{\mathrm{bb}} \sim 6600$ K) but larger radius ($R_{\mathrm{bb}} \sim 3 \times 10^{15}$ cm).

(ii) During the main peak phase, which lasts 180 d (AT2024kmq) and 290 d (AT2024lhc) in the rest frame, both events maintain relatively constant temperatures of $T_{\mathrm{bb}} \sim 2 \times 10^4$ K. The maximum radius is $R_{\mathrm{bb}} \sim 10^{15}$ cm $\sim 70 r_{\mathrm{g}} M_{\mathrm{BH},8}^{-1}$ (see equation 2). Their peak luminosities ($L_{\mathrm{bb}} \sim 10^{44.5}$ erg s^{-1}) are at the high-end of the TDE population (Y. Yao et al. 2023). Each event shows a sharp drop at the end of this phase driven by the decreasing R_{bb}.

(iii) Additionally, beginning at $t_{\mathrm{rest}} \approx 310$ d, AT2024kmq exhibits a rebrightening phase, which appears to have ended by $t_{\mathrm{rest}} \approx 480$ d.

We discuss the possible power sources of the UV/optical emission during and after the precursor in Sections 4.3 and 4.4, respectively.

3.7 *Hubble Space Telescope* UV spectroscopy

We obtained eight orbits of UV spectroscopy of AT2024lhc with the Space Telescope Imaging Spectrograph (STIS; B. E. Woodgate et al. 1998) MAMA detectors onboard the *Hubble Space Telescope* (*HST*) (GO-17767; PI: Chornock) on 2025 June 5 and 6 ($t_{\mathrm{rest}} \approx 338$ d). The original observation plan included four orbits of far-UV (FUV) spectroscopy with the G140L grism and four orbits of near-UV (NUV) spectroscopy with the G230L grism spread over three visits. However, two of the visits suffered guide star failures, and usable data were obtained for three orbits of G140L observations and one orbit of G230L, for total exposure times of 7199 s and 1919 s in the FUV and NUV, respectively. In addition, between triggering and acquisition of the observations, AT2024lhc faded significantly (Fig. 1). The resultant low signal-to-noise ratio (SNR) of the observations caused the default pipeline reduction to misidentify the object trace in two exposures. We manually re-ran the `x1d` pipeline extraction with the `A2CENTER` parameter set to

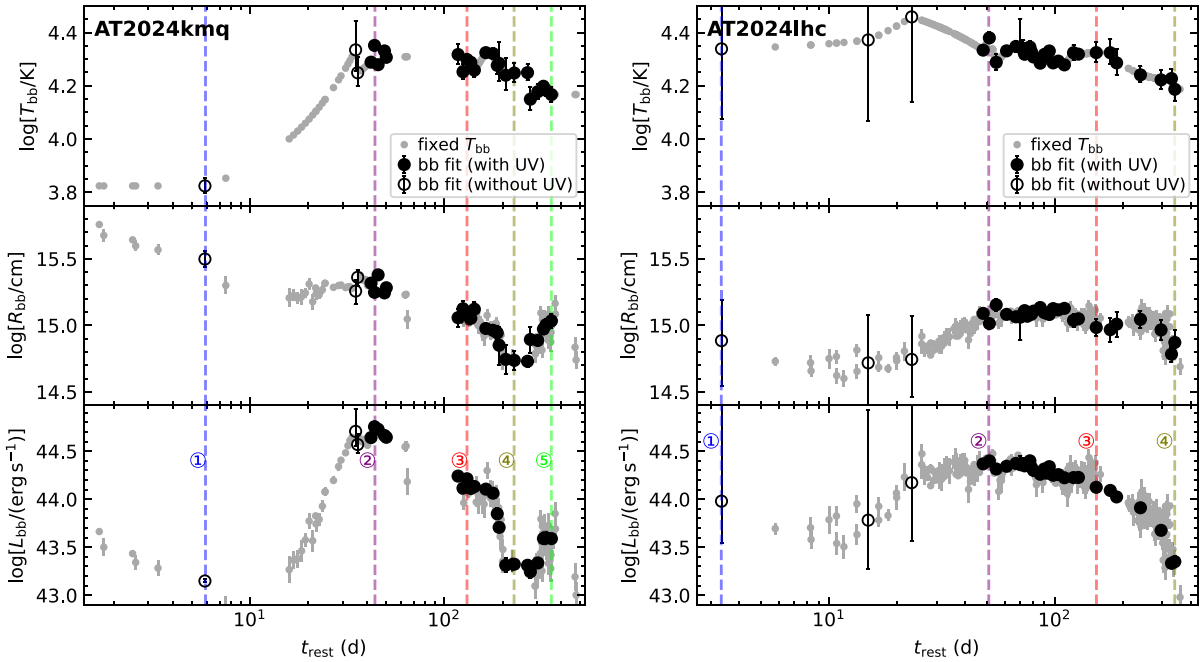

Figure 9. Evolution of the UV/optical blackbody properties of AT2024lhc and AT2024kmq. Epochs where both $T_{\rm bb}$ and $R_{\rm bb}$ are fitted are shown in black, where solid and hollow markers indicate epochs with and without UVOT observations, respectively. Epochs scaled assuming fixed $T_{\rm bb}$ are shown in grey. The vertical dashed lines mark epochs where detailed broad-band SEDs are presented in Fig. 11.

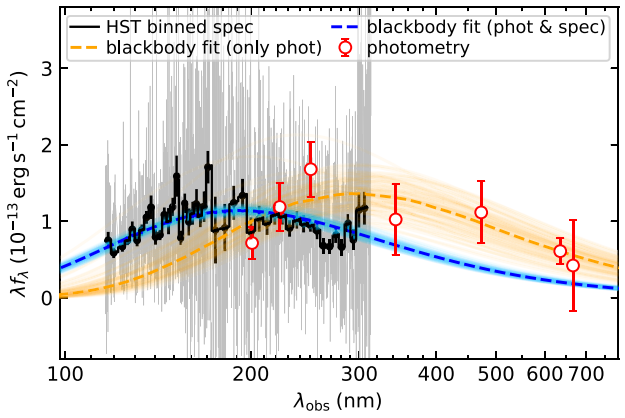

Figure 10. *HST* UV spectrum of AT2024lhc. The unbinned and binned data are shown in thick black and thin grey lines, respectively. Regions affected by strong geocoronal absorption or emission have been masked. The blue lines show the blackbody model fitted to both spectroscopy and photometry, while the orange lines show the model fitted to photometry only.

be near the actual location of the source. The individual object exposures were combined using the Hubble Advanced Spectral Products (HASP; J. Debes et al. 2024) script using default parameters.

The final *HST* spectrum is shown in Fig. 10. The grey line shows the raw data, and the black line shows the binned spectrum. We binned the spectra by a factor of 40 pixels, where each binned flux value is the mean of 40 consecutive pixels, and the flux uncertainty is estimated as the standard error of the mean within each bin. The red data show the UV and optical photometry obtained at $t_{\rm rest} = 340.3$ d, which is very close in time to the *HST* observation. We see that in the NUV band where both photometry and spectrum are available, the data are consistent with each other at the $< 2\sigma$ level.

To assess whether the blackbody function employed in Section 3.6 also provides a good description of the FUV data, in Fig. 10, we show the best-fitting blackbody model obtained in Section 3.6 using the dashed thick orange line, and 100 random draws from the MCMC posterior using the solid thin orange lines (see Section 3.6). As can be seen, when fitting only to photometry, the blackbody model, with $\log(T_{\rm bb}/{\rm K}) = 4.18^{+0.05}_{-0.04}$ and $\log(R_{\rm bb}/{\rm cm}) = 14.99^{+0.09}_{-0.10}$, systematically underestimates the FUV flux at $\lambda_{\rm obs} < 1700$ Å. When we instead fit the blackbody model to both the *HST* spectroscopy and photometry simultaneously, we obtain $\log(T_{\rm bb}/{\rm K}) = 4.36 \pm 0.01$ and $\log(R_{\rm bb}/{\rm cm}) = 14.48^{+0.03}_{-0.02}$, shown as blue lines in Fig. 10. We note that because the photometric uncertainties are large, this joint fit is effectively dominated by the *HST* spectrum. This fit slightly underestimates the optical photometry, though the discrepancy remains within the photometric uncertainties.

Our *HST* observations therefore suggest that the blackbody parameters derived in Section 3.6 should be taken with caution, and that a single blackbody might not provide an adequate description of the underlying intrinsic FUV–optical SED shape.

3.8 Broad-band SED

We construct broad-band SEDs from the radio to hard X-ray bands at representative epochs in the light curve evolution (marked by vertical dashed lines in Fig. 9). Fig. 11 shows the SEDs at each epoch, comprising: available radio upper limits, UV/optical photometry with the 68 per cent confi-

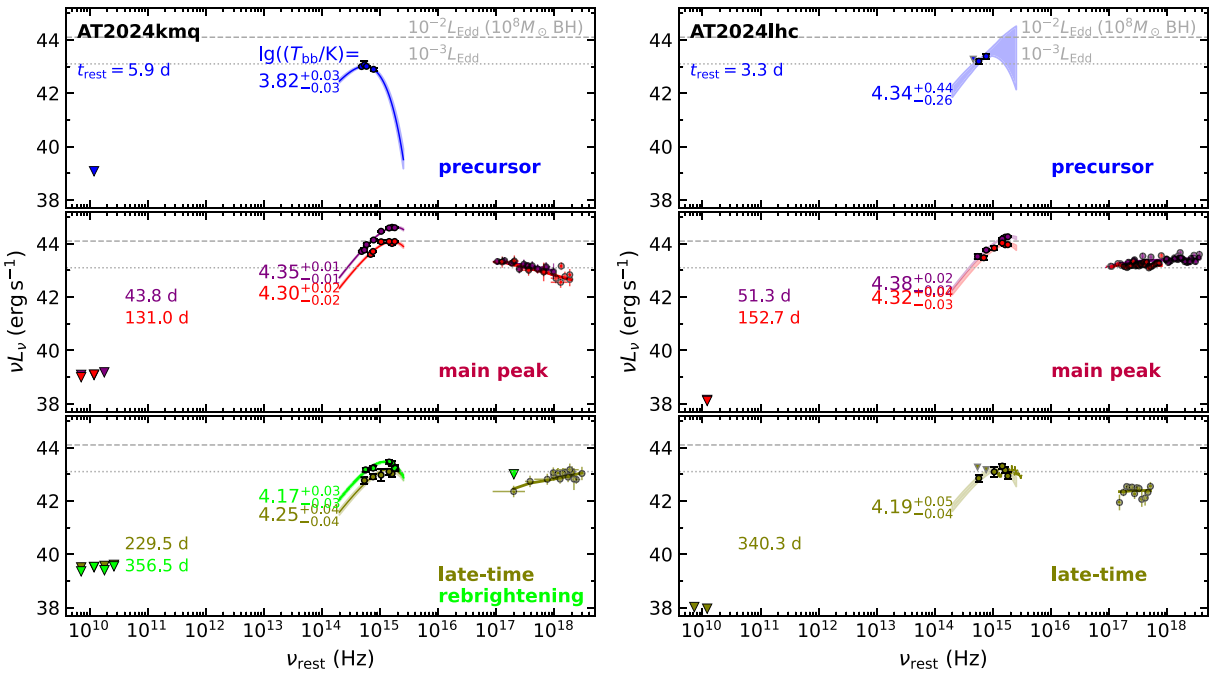

Figure 11. Broad-band SEDs of AT2024kmq and AT2024lhc at representative epochs. In each panel, the horizontal dashed and dotted lines show $10^{-2}L_{\rm Edd}$ and $10^{-3}L_{\rm Edd}$ for 10^8 $M_\odot$ BHs, where $L_{\rm Edd} = 1.26 \times 10^{38}(M_{\rm BH}/M_\odot)\,{\rm erg\,s^{-1}}$.

dence interval of the blackbody fits, and X-ray spectra or upper limits.

We compute the bolometric luminosity following Y. Yao et al. (2022). The rest-frame spectrum is divided into three frequency ranges: (1) Between $\nu_{\rm rest} = 10^{14}$ and $10^{15.5}$ Hz, we integrate beneath the blackbody model fitted to UV/optical photometry (Section 3.6). (2) Between $\nu_{\rm rest} = 10^{17}$ and $10^{18.5}$ Hz, we integrate beneath the best-fitting X-ray spectral model (Section 3.4). (3) Between $\nu_{\rm rest} = 10^{15.5}$ and 10^{17} Hz (the EUV gap), we assume the spectrum is continuous and approximate it with a power law connecting the UV and X-ray components. When X-ray observations are unavailable or yield only upper limits, we exclude the X-ray and EUV components, treating the UV/optical integral as a lower limit on $L_{\rm bol}$.

Table 3 presents the computed bolometric luminosities and the corresponding Eddington ratios $\lambda_{\rm Edd} \equiv L_{\rm bol}/L_{\rm Edd}$.

4 DISCUSSION

Here, we discuss AT2024kmq and AT2024lhc in the context of spectroscopically featureless TDEs. In Section 4.1, we examine the optical properties and BH masses of featureless TDEs in comparison to broad-line TDEs. We then discuss the origin of their X-ray emission in Section 4.2, the optical precursor emission in Section 4.3, and the post-precursor UV/optical emission in Section 4.4.

4.1 Featureless blue TDEs: two sub-classes?

To place AT2024kmq and AT2024lhc in the context of known spectroscopically featureless TDEs, we compile a sample of ZTF TDEs. We start with 46 TDEs with known spectroscopic subtypes from ZTF sample papers (E. Hammerstein et al. 2023a; Y. Yao et al. 2023, 2025), excluding AT2021qth/ZTF21abhrchb (the only TDE-coronal source) and AT2021gje/ZTF21aapvvtb (an event with peculiar spectral features). We also include two events classified as TDE-featureless (AT2022gri/ZTF20aahmtso, AT2019wzc/ZTF19acnskyy/Ansky) by J. Zhu et al. (2025), and AT2020ohl/ASASSN-20hx/ZTF20abjpxei, previously classified as an ambiguous nuclear transient (ANT) by J. T. Hinkle et al. (2022). We reclassify AT2020ohl as TDE-featureless because, unlike other ANTs (see examples in S. Frederick et al. 2021; P. Wiseman et al. 2025), it lacks broad Balmer lines and exhibits a featureless blue continuum throughout its evolution, similar to AT2022gri and AT2019wzc. It is also the only source among 19 ANTs examined by J. T. Hinkle (2024) that lacks a dust reprocessing echo.

This gives us a comparison sample of 49 TDEs. The number of events in each spectral sub-type is given in Table 4. We characterize their UV and optical light curves following the same procedures as outlined in Y. Yao et al. (2023). The light curve properties we measure are UV/optical blackbody luminosity and radius ($L_{\rm bb}$ and $R_{\rm bb}$) at light curve maximum. Of the 49 TDEs in our sample, 29 have published velocity dispersion measurements (R. Ahumada et al. 2020; E. Hammerstein et al. 2023b; Y. Yao et al. 2023, 2025), to which we add AT2022gri with $\sigma_* = 155 \pm 4$ km s^{-1} derived from our analysis of its DESI spectrum. For these 30 objects, we apply the J. Kormendy & L. C. Ho (2013) $M_{\rm BH}$–σ_* relation. For the remaining 19 TDEs without velocity dispersion measurements, we use the $M_{\rm BH}$–$M_{\rm gal}$ scaling relation (equation 5 of Y. Yao et al. 2023).

Fig. 12 presents the comparison sample across $M_{\rm BH}$, $L_{\rm bb}$, and $R_{\rm bb}$, as well as the distributions. Because individual BH mass estimates for TDE hosts carry large uncertainties, we represent the $M_{\rm BH}$ distributions using kernel density estimation with bandwidths set by the measurement uncertainties. In contrast, the

Table 3. Bolometric luminosity at representative phases.

Name	$t_{\rm rest}$ (d)	$L_{\rm bol}$ (erg s^{-1})	$\lambda_{\rm Edd}$ [a]	$\lambda_{\rm Edd}$ [b]
2024kmq	5.9	$> 1.5 \times 10^{43}$	$> 6.0 \times 10^{-4}$	$> 2.6 \times 10^{-3}$
	43.8	1.1×10^{45}	4.4×10^{-2}	0.19
	131.0	3.7×10^{44}	0.015	0.064
	229.5	5.2×10^{43}	2.1×10^{-3}	9.0×10^{-3}
	356.5	$> 3.9 \times 10^{43}$	$> 1.6 \times 10^{-3}$	$> 6.8 \times 10^{-3}$
2024lhc	3.3	$> 3.3 \times 10^{43}$	$> 4.6 \times 10^{-4}$	$> 3.1 \times 10^{-3}$
	51.3	5.2×10^{44}	7.2×10^{-3}	0.048
	152.7	3.5×10^{44}	4.8×10^{-3}	0.033
	340.3	4.8×10^{43}	6.6×10^{-4}	4.4×10^{-3}

Note.[a] Eddington ratio adopting $M_{\rm BH}$ estimated from σ_*, see Table 1. [b] Eddington ratio adopting $M_{\rm BH}$ estimated from TIDALSPIN, see Table 1.

Table 4. Bootstrap bimodality test using the comparison sample.

Spectral sub-type	$N_{\rm TDE}$ [a]	$\log[L_{\rm bb}/({\rm erg\,s^{-1}})]$ [b] (per cent)	$\log[R_{\rm bb}/{\rm cm}]$ [b] (per cent)
TDE-H + He	24	0.0	0.2
TDE-H	9	2.4	52.6
TDE-He	5	– [c]	43.0
TDE-featureless	11	100.0	86.8

Note.[a] Number of TDEs in each spectral type. [b] The fraction of 1000 bootstrap realizations that satisfy both conservative bimodality criteria (silhouette score > 0.7 and Cohen's $d > 3.0$) for each spectral sub-type and observable. [c] Cohen's d cannot be reliably computed in the majority of bootstrap realizations because one of the two clusters contains fewer than two events.

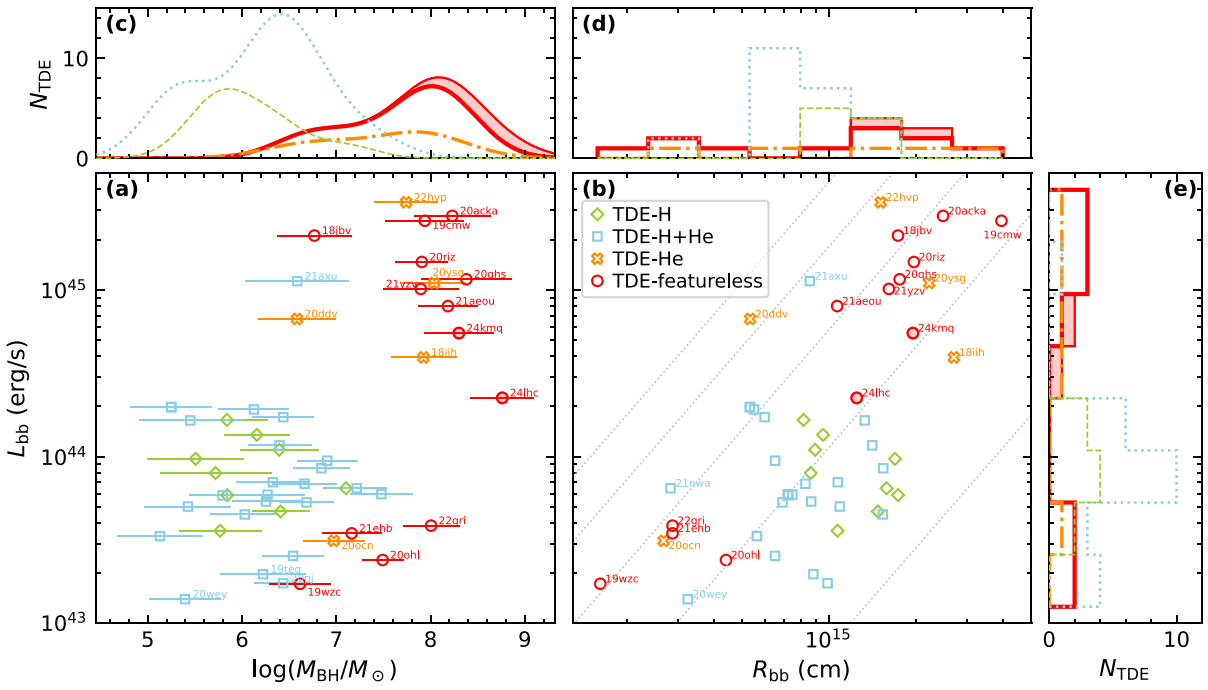

Figure 12. AT2024kmq and AT2024lhc compared with other TDEs, colour-coded by spectral sub-classes. Panel (a): TDEs in the phase space of peak $L_{\rm bb}$ and black hole mass, where $M_{\rm BH}$ is directly estimated using host-galaxy scaling relations. Panel (b): TDEs in the phase space of peak $L_{\rm bb}$ and $R_{\rm bb}$ at peak luminosity. Dotted lines show constant temperatures of $T_{\rm bb} = [1, 2, 3, 4, 5] \times 10^4$ K. Panel (c): Distribution of $M_{\rm BH}$ for TDEs of four spectral sub-classes, estimated using kernel density estimation with bandwidth equal to the uncertainty in $M_{\rm BH}$. Panels (d) and (e): Histograms of $L_{\rm bb}$ and $R_{\rm bb}$ at maximum light for the four spectral sub-classes. For the TDE-featureless class (panels c–e), thin red lines show the results including AT2024kmq and AT2024lhc, while thick red lines show the distribution of the comparison sample only. The red shaded regions indicate the contribution of these two events.

uncertainties on $L_{\rm bb}$ and $R_{\rm bb}$ at peak are relatively small, so simple histograms provide an adequate representation of their distributions. Similar to what was reported in E. Hammerstein et al. (2023a), we see that the TDE-featureless and TDE-He sub-types are generally hosted by higher-mass BHs, and they also exhibit higher peak blackbody temperatures compared to the TDE-H and TDE-H + He sub-types.

Before discussing the distributions of the blackbody parameters in detail, we first caution that a single blackbody may not provide an adequate description of the TDE UV/optical continuum SED shape. As shown in Section 3.7 and in multiple previous studies (S. B. Cenko et al. 2016; S. van Velzen et al. 2020; T. Hung et al. 2021; J. Zhu et al. 2025), a single-temperature blackbody fit to NUV and optical photometry often underestimates the FUV continuum. Nevertheless, the blackbody function has the advantage of simplicity and provides estimates of the characteristic size and temperature of the UV/optical emitting region, albeit with systematic uncertainties.

With this caveat in mind, we note that the TDE-featureless class appears bimodal in peak $L_{\rm bb}$ (panel e): one population has $2 \times 10^{44} \lesssim [L_{\rm bb}/({\rm erg\,s^{-1}})] \lesssim 3 \times 10^{45}$, and another has $10^{43} \lesssim [L_{\rm bb}/({\rm erg\,s^{-1}})] \lesssim 4 \times 10^{43}$. This bimodality is also evident in $\log[R_{\rm bb}/({\rm cm})]$ (panel d).

To assess bimodality robustness, we perform a conservative bootstrap analysis using K-means clustering. For each spectral subtype, we perform 1000 bootstrap iterations where each data point is perturbed by Gaussian noise ($\sigma = 0.05$ dex for $\log T_{\rm bb}$ and $\sigma = 0.02$ dex for $\log R_{\rm bb}$)[5] to account for measurement uncertainties. In each iteration, we fit a two-component K-means model and compute: (1) the silhouette score,[6] which quantifies cluster quality by measuring how well-separated points are between clusters relative to their dispersion within clusters, and (2) the separation ratio (Cohen's d),[7] defined as the distance between cluster centers divided by the pooled within-cluster standard deviation. We impose stringent dual criteria for claiming bimodality: silhouette score > 0.7 (indicating excellent cluster separation) and separation ratio >3.0 (indicating clusters separated by more than 3σ). A distribution is classified as robustly bimodal only if >80 per cent of bootstrap samples simultaneously satisfy both criteria.

Table 4 presents the results using only the comparison sample of 49 TDEs. The TDE-featureless class exhibits robust bimodality in both $\log L_{\rm bb}$ (100.0 per cent of bootstrap samples) and $\log R_{\rm bb}$ (86.8 per cent), while all other spectral subtypes are consistent with unimodal distributions. Including AT2024kmq and AT2024lhc in the test leads to slightly different fractions: $\log L_{\rm bb}$ (99.9 per cent of bootstrap samples) and $\log R_{\rm bb}$ (93.5 per cent), and evidence for bimodality remains strong. We caution that given the small sample size and potential selection biases, this bimodal structure should be validated with larger, systematically selected samples in future work.

The bimodality seen among the TDE-featureless class may be closely connected to the physical conditions required to suppress line formation in luminous transients. In particular, the radiative transfer models of O. Aspegren & D. Kasen (2026) show that featureless blue spectra can arise in multiple regimes that lead to high ionization. The ionization state is set by the Saha equation, which depends on the temperature – the hotter the medium, the more ionized it is – so sustaining high temperatures is key to suppressing line formation. Within this framework, the two subclasses we identify may represent two ways that inhibit line formation: a high source luminosity regime (where AT2024kmq and AT2024lhc reside) and a compact photosphere regime (containing AT2019wzc, AT2020ohl, AT2021ehb, and AT2022gri). Consistent with this interpretation, panel (b) of Fig. 12 shows that the TDE-featureless and TDE-He sub-types generally exhibit higher peak blackbody temperatures compared to the TDE-H + He subtype, with the TDE-H sub-type exhibiting the lowest temperatures.

Higher-mass BHs may also favour featureless spectra since stronger GR effects could boost outflow velocities, which help suppress intrinsically strong UV metal lines (O. Aspegren & D. Kasen 2026). Indeed, J. Zhu et al. (2025) presented *HST* UV spectra of three sub-luminous featureless TDEs (AT2019wzc, AT2021ehb, AT2022gri), demonstrating their lack of spectral features even in the UV. This suggests that high outflow velocities may also play a role in establishing featureless spectra. The *HST* UV spectrum of AT2024lhc presented here is not of high enough SNR to search for spectral lines – future UV spectroscopy studies of luminous featureless TDEs will be useful to test this hypothesis.

4.2 Origin of the TDE hard X-ray emission

A common behaviour between AT2024kmq and AT2024lhc is their luminous ($L_{\rm X,peak} \sim 10^{44}\,{\rm erg\,s^{-1}}$) X-ray emission appearing at early times. Their peak X-ray luminosities exceed the pre-flare host galaxy levels (Table 1) by more than two orders of magnitude, ruling out contamination from pre-existing AGNs. The X-ray spectral hardness is inconsistent with thermal emission from an accretion disc. In both events, NuSTAR detects high-energy photons extending to ∼20 keV (Fig. A1).

The minimum detected X-ray variability time-scales are 1.3 and 4.8 h for both AT2024kmq and AT2024lhc, respectively (see Table 2), providing upper limits on the intrinsic variability time-scales. For a $10^8\,{\rm M_\odot}$ BH, this corresponds to ~ 10 light-crossing times of the gravitational radius ($t_{\rm g} = r_{\rm g}/c \approx 500$ s). The rapid X-ray variability therefore constrains the X-ray emitting region to $\lesssim 10 r_{\rm g}$. This strongly suggests a compact emitting region. The absence of radio detections of the transients out to $t_{\rm rest} \sim 1$ yr (Section 3.5) disfavours a jet, though a highly off-axis configuration (I. Sfaradi et al. 2024) cannot be excluded.

Power-law X-ray continua can arise from two primary mechanisms: thermal Comptonization, in which soft disc photons are inverse Compton scattered by thermal electrons in a hot, optically thin, compact corona (R. A. Sunyaev & L. G. Titarchuk 1980), or bulk Comptonization, in which photons are upscattered by electrons with non-uniform transrelativistic bulk motions (R. D. Blandford & D. G. Payne 1981). In AGNs and XRBs, thermal Comptonization dominates (M. Gilfanov & A. Merloni 2014; E. Kara & J. García 2025), though recent three-dimensional radiation magnetohydrodynamic simulations of AGN and TDE environments suggest bulk Comptonization may also contribute (Y.-F. Jiang et al. 2025; X. Huang et al. 2025).

The broad-band spectrum shape of both events during their main peaks are similar to those found in recent simulations

[5]These are the medians of measurement uncertainties (see e.g. table 6 of E. Hammerstein et al. 2023a). We have verified that choosing slightly different values of σ does not significantly change the results of our analysis.
[6]https://en.wikipedia.org/wiki/Silhouette_(clustering)
[7]https://en.wikipedia.org/wiki/Effect_size#Cohen's_d

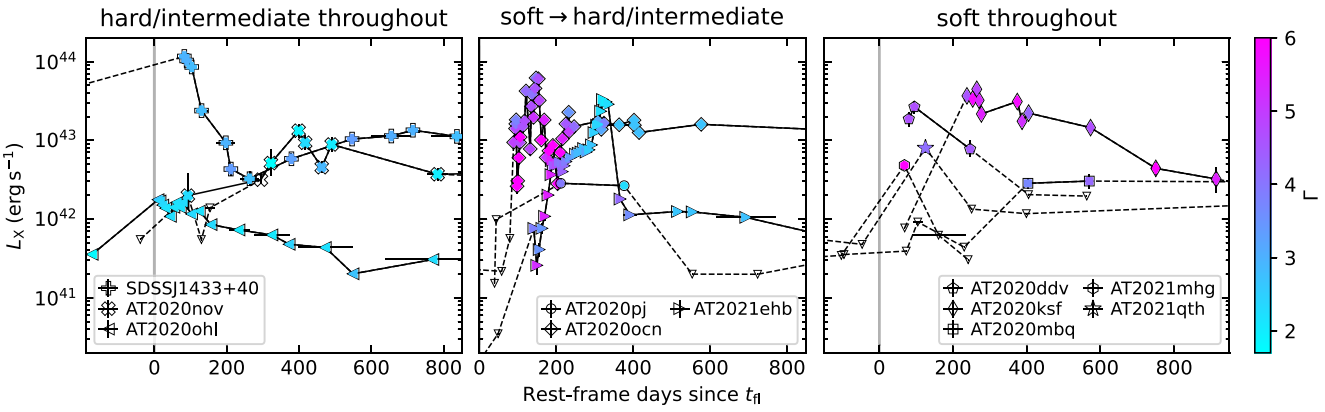

Figure 13. X-ray light curves of 11 ZTF TDEs with eROSITA detections within 6 months after first optical light. The data points are colour-coded by the X-ray spectral power-law index Γ.

due to bulk Comptonization (X. Huang et al. 2025). However, AT2024kmq exhibits a hard X-ray photon index at late times ($\Gamma \approx 1.6$; Fig. 2, Table B2), whereas the spectrum shape produced by bulk Comptonization is sensitive to local velocity field and rarely produce photon index of $\Gamma < 2$ (R. D. Blandford & D. G. Payne 1981). We will later show that thermal Comptonization naturally explains why hard X-rays are preferentially detected in high-$M_{\rm BH}$ TDEs (see below). Note that in the accretion disc plus corona geometry, one would expect reflection features (e.g. relativistically broadened iron line and Compton hump; A. C. Fabian 2016) to be present. However, the faintness of these TDEs precludes detection of such features in our NuSTAR observations.

Previous X-ray studies of non-jetted TDEs have established that their emission is typically soft and consistent with thermal disc emission (K. Auchettl, J. Guillochon & E. Ramirez-Ruiz 2017; S. Sazonov et al. 2021; M. Guolo et al. 2024). In some cases (e.g. AT2018fyk, AT2020ocn, and AT2021ehb), a spectral state transition of soft → hard (or soft → intermediate) have been observed at a few hundred days after the optical peak, which has been interpreted as coming from inverse Compton scattering of thermal disc photons in a region of hot corona (T. Wevers et al. 2021; Y. Yao et al. 2022; M. Guolo et al. 2024). Y. Yao et al. (2022) postulated that in those events, a few hundred days is needed for the magnetic field to build up via differential rotation, which then leads to a magnetically dominated hot corona. In ASASSN-15oi, the soft → hard transition occurred around $\sim 10^3$ d (A. Hajela et al. 2025).

In contrast, AT2024kmq and AT2024lhc exhibit hard X-ray emission at much earlier times ($t_{\rm rest} < 50$ d or no later than the optical peak), raising the question: what physical conditions enable rapid corona formation? To address this, we next contextualize our events within a control sample of ZTF TDEs with early-time X-ray constraints, and compare observations with accretion disc theories.

4.2.1 *Evidence for soft-to-hard state transition at $\dot{m} = 0.03$*

We utilize X-ray data from the eROSITA-RU covering Galactic longitudes $0^\circ < l < 180^\circ$. During its all-sky surveys (December 2019–February 2022, with 6-month cadence), eROSITA provides unbiased X-ray snapshots for ZTF TDEs. We selected all publicly classified TDEs passing the ZTF TDE selection filter (S. van Velzen et al. 2021) with at least one eROSITA observation between first optical light $t_{\rm fl}$ and 6 months after $t_{\rm fl}$. This yields a comparison sample of 30 TDEs constructed without prior knowledge of X-ray properties. Following the procedures adopted in Section 4.1, we estimate the BH masses of this comparison sample[8] using host-galaxy scaling relations: the $M_{\rm BH}$–σ_* relation for galaxies with measured velocity dispersions, and the $M_{\rm BH}$–$M_{\rm gal}$ relation otherwise. We cross-matched this sample with the eROSITA source catalogue, resulting in 11 TDEs with matched sources. The eROSITA upper limits of the remaining 19 sources are all $< 10^{43}$ erg s^{-1}.

In Fig. 13, we show the detailed X-ray (eROSITA + *Swift*/XRT) light curves of the 11 detected sources, colour-coded by Γ. All X-ray spectra were modelled using `tbabs*zashift*powerlaw` following the same procedures outlined in Section 3.4.1. For ZTF19acymzwg (SDSS J1430+43), we further added a component of host absorption (`ztbabs`) with $N_{\rm H,host}$ fixed at 7×10^{20} cm^{-2}, following M. Brightman et al. (2021). Based on the values of Γ, we divide the X-ray states into soft ($\Gamma > 4$), intermediate ($\Gamma \sim 3$), and hard ($\Gamma \lesssim 2.5$). As indicated by Fig. 13, the X-ray spectral evolution of the 11 TDEs with eROSITA detections can generally be divided into three categories: those with soft spectra throughout the first ~ 2 yr, those with hard/intermediate spectra throughout the first ~ 2 yr, and those with a spectral transition of soft → hard/intermediate around ~ 1 yr.

In Fig. 14, we show the distribution of the comparison sample in the $M_{\rm g,peak}$ vs. $M_{\rm BH}$ diagram, colour-coded by the X-ray spectral class. One striking result is the mass segregation of those TDEs that have X-ray spectra which are always soft (lowest masses), transition between states (middle masses) and are always hard (highest masses). We caution that if we attribute the soft component to a thermally emitting disc, then at fixed Eddington ratio, the peak disc temperature $T_{\rm p} \propto M_{\rm BH}^{-1/4}$, such that at sufficiently high BH masses ($M_{\rm BH} \gtrsim 10^7$ M$_\odot$), the Wien tail of the disc spectrum is not expected to produce detectable soft X-ray emission (see e.g. fig. 5 of M. Guolo et al. 2025). It is therefore not surprising that there exist no events with $M_{\rm BH} \sim 10^8$ M$_\odot$ classified in the

[8]We note that M. Brightman et al. (2021) reported $\sigma_* = 213 \pm 12$ km s^{-1} for ZTF19acymzwg (SDSS J1430+43) using a Keck/LRIS spectrum, which does not have the resolution to measure σ_*. We therefore exclude this measurement and estimate the black hole mass from its $M_{\rm gal}$ instead.

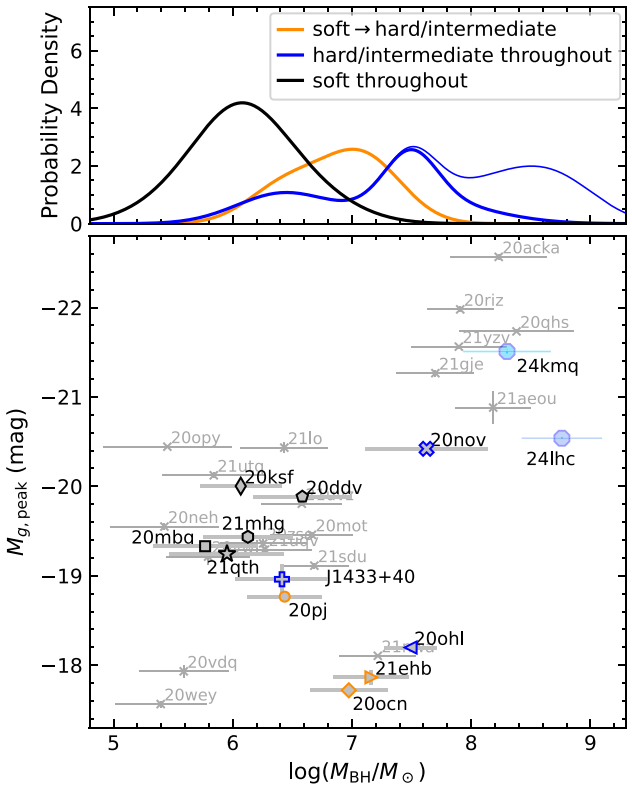

Figure 14. *Upper*: Black hole mass distribution of X-ray detected TDEs obtained by kernel density estimation, using a kernel width equal to the uncertainty of M_{BH}. For the 'hard/intermediate throughout' class, the thin blue line shows the result including AT2024kmq and AT2024lhc, while the thick blue line shows the result with the comparison sample only. *Bottom*: Peak rest-frame *g*-band luminosity versus black hole mass for AT2024kmq, AT2024lhc, and the comparison sample, where M_{BH} is estimated using host-galaxy scaling relations. Markers follow the same scheme as in Fig. 13. We caution that for BH masses $\gtrsim 10^7\,\mathrm{M}_\odot$, the peak of the disc thermal emission falls below the observable X-ray band.

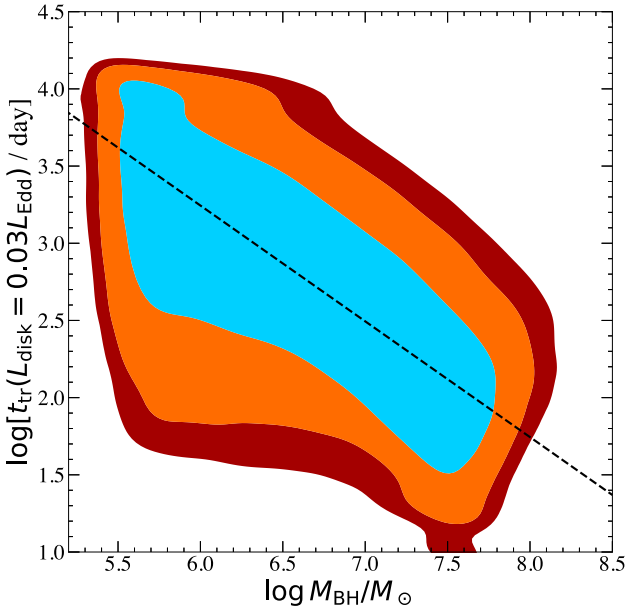

Figure 15. The time for a variety of different simulated TDE disc systems to fall to an Eddington ratio of 0.03 (see the text for simulation details), as a function of black hole mass. The blue, orange, and red contours show 1σ, 2σ, and $3\,\sigma$ confidence intervals respectively (i.e. they contain 68.3 per cent, 95.4 per cent and 99.7 per cent of the points). The black dashed curve shows the analytical scaling argument discussed in the text $t_{\mathrm{tr}} \propto M_{\mathrm{BH}}^{-3/4}$. We see that the analytical argument captures the main trend across the simulated population. The vast majority of sources with black holes mass $M_{\mathrm{BH}} \gtrsim 10^8\,\mathrm{M}_\odot$ did not ever exceed an Eddington ratio of 0.03, and are not displayed.

soft-only class. However, if those high-M_{BH} TDEs transition to the hard state during later phases of the flare evolution, they should produce detectable hard X-ray emission.

This mass segregation of the X-ray spectral states of TDEs was predicted by A. Mummery & S. A. Balbus (2021a). It can be understood with classical time-dependent accretion disc theory, and the additional assumption that TDE discs transition to a harder accretion state at a fixed $\dot{m}$. Heuristically, note that the viscous time-scale in a TDE disc is (to leading order) independent of BH mass

$$t_{\mathrm{visc}} \approx \alpha^{-1}(h/r)^{-2}\sqrt{r_{\mathrm{T}}^3/GM_{\mathrm{BH}}} \approx \alpha^{-1}(h/r)^{-2}\sqrt{R_\star^3/GM_\star}, \tag{4}$$

where h/r is the aspect ratio of the disc. We assume that a fraction f_{d} of the returning stellar material which forms a disc, such that $M_{\mathrm{disc}} = f_{\mathrm{d}}M_\star$ does not depend on M_{BH}. Thus, the peak accretion rate (in unit of $\dot{M}_{\mathrm{Edd}}$) of a TDE disc is generically a decreasing function of BH mass

$$\dot{m}_{\mathrm{peak}} \equiv \frac{\dot{M}_{\mathrm{acc,peak}}}{\dot{M}_{\mathrm{Edd}}} \approx \frac{M_{\mathrm{disc}}}{t_{\mathrm{visc}}} \times \frac{1}{\dot{M}_{\mathrm{Edd}}} \propto \frac{1}{M_{\mathrm{BH}}}. \tag{5}$$

With a lower $\dot{m}_{\mathrm{peak}}$ and a similar evolutionary time-scale, higher mass BH TDEs will have $\dot{m}_{\mathrm{peak}} \sim 0.01$ at earlier times, making them more likely to be represented in a sample of TDEs with coronae. Conversely, lower-mass BHs will stay above a given Eddington accretion ratio for longer.

The above heuristic argument can be made quantitative. Indeed, A. Mummery (2026) calculated the time it takes for a TDE disc accretion rate to drop to a certain value of $\dot{m}$, which we denote t_{tr}. For a full disruption, the transition time is

$$t_{\mathrm{tr}} \approx 4000\,\mathrm{d}\,\alpha_{-1}^{-1/4}\theta_{-1}^{-1/2}\eta_{-1}^{3/4}f_{\mathrm{d},-1}^{3/4}m_\star^{5/8}r_\star^{3/8}\dot{m}_{-2}^{-3/4}M_{\mathrm{BH},6}^{-3/4}. \tag{6}$$

Here, η is the radiative efficiency of the accretion disc, $m_\star \equiv M_\star/\mathrm{M}_\odot$, $r_\star \equiv R_\star/R_\odot$, and $\theta \equiv (h/r)$. A subscript $-1\,(-2)$ indicates that a value has been normalized by 0.1 (0.01), respectively. The mass-segregation of the different spectral states can then be understood from the $t_{\mathrm{tr}} \propto M_{\mathrm{BH}}^{-3/4}$ scaling of the time to fall to a fixed value of $\dot{m}$.

To verify this quantitatively, we perform a numerical population synthesis calculation of the time required to reach $\dot{m} = 0.03$. This threshold is motivated by observations of BH XRBs (see Section 1). We sample BH masses from a log-uniform distribution spanning $10^{5.5}$–$10^{8.5}\mathrm{M}_\odot$ and, for each BH mass, draw stellar,[9] and disc properties following A. Mummery et al. (2024). For every sampled system, we solve the time-dependent disc equations using the FITTED code (A. Mummery et al. 2025a) to compute the transition time t_{tr} at which the disc bolometric luminosity reaches $0.03L_{\mathrm{Edd}}$. Fig. 15 shows the resulting distribution of M_{BH} versus t_{tr} from $N = 10^5$ simulated systems. The black dashed

[9]Note that for modelling convenience, our simulated sample does not include partial disruptions with $\beta < 1$, where β is defined as the ratio between the pericenter distance and the tidal radius.

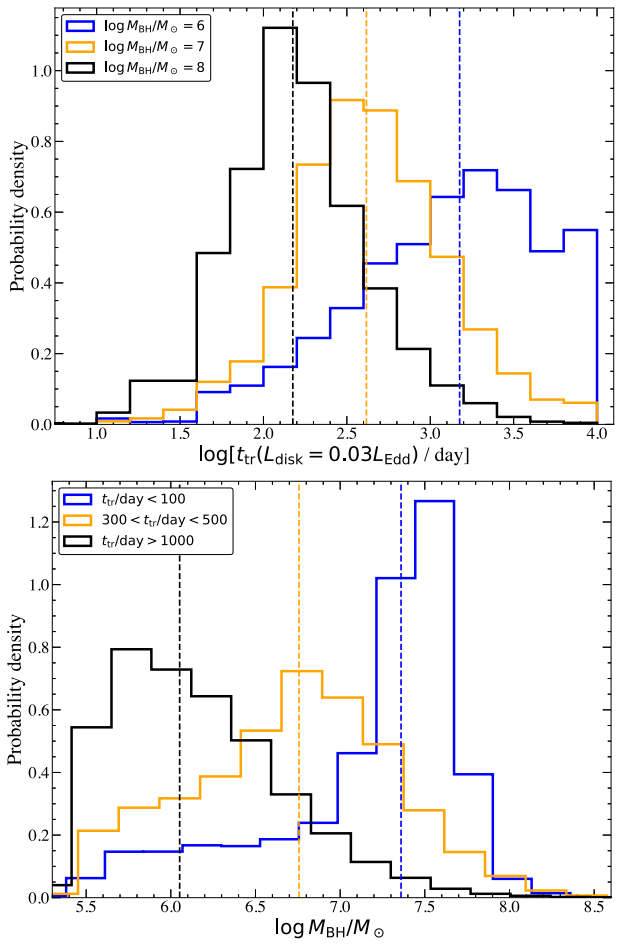

Figure 16. *Upper*: One-dimensional probability distributions of the transition time for disc systems within a factor 2 of the black hole masses denoted on the plot. We see that $M_{BH} \sim 10^6 M_\odot$ TDE systems typically take $\sim 10^3$ d (multiple years), $M_{BH} \sim 10^7$ M$_\odot$ systems typically transition after ~ 1 yr, while $M_{BH} \sim 10^8$ M$_\odot$ systems transition rapidly at $t \lesssim 100$ d, and will likely only ever be observed in a harder state. *Lower*: One-dimensional projection of the black hole masses for systems which transition through $\dot{m} = 0.03$ in different temporal bins: rapidly $t_{tr} < 100$ d (blue posterior), on intermediate time-scales $t_{tr} \in (300, 500)$ d (orange posterior), and on long time-scales $t_{tr} > 10^3$ d. These posteriors are in good agreement with that seen in the data (upper panel of Fig. 14).

curve shows the analytical prediction from equation (6), which accurately captures the mean trend and validates the $t_{tr} \propto M_{BH}^{-3/4}$ scaling.

To elucidate the mass-dependent transition behaviour, we project the two-dimensional M_{BH}–t_{tr} distribution (Fig. 15) onto one-dimensional posteriors. In Fig. 16, the upper panel shows the distribution of transition times for systems within three narrow (within ± 0.1 dex) mass bins ($M_{BH} = 10^6$, 10^7, and 10^8M$_\odot$); the lower panel shows the BH mass distributions for systems transitioning within specific time windows (early: $t_{tr} <$ 100 d; intermediate: 300–500 d; late: $>$ 1000 d), which closely match the observed mass segregation in X-ray spectral states (Fig. 14, upper panel). These distributions demonstrate that simple time-dependent disc theory quantitatively reproduces the data.

We note again that at fixed Eddington ratio, higher-mass BHs produce cooler accretion discs whose peak thermal emission lies below the soft X-ray band. A. Mummery & S. A. Balbus (2021b) showed that above a critical mass $M_{crit} \sim 2 \times 10^7M_\odot$, TDE discs become increasingly unlikely to produce detectable thermal X-ray emission, as the disc emission peaks in the EUV band. Consequently, even if a $M_{BH} \sim 10^8$M$_\odot$ TDE remains above the $\dot{m} \sim 0.03$ threshold and has not yet formed a corona, it would likely evade detection in soft X-ray surveys. However, once these high-mass systems transition into the hard (coronal) state, they will become X-ray detectable again. Among the five TDEs in the 'hard/intermediate throughout' X-ray sub-class (namely SDSSJ1433+40, AT2020nov, and AT2020ohl in the control sample, as well as AT2024kmq and AT2024lhc), the earliest post-discovery X-ray observations already reveal hard-state detections (instead of upper limits), indicating that the corona formed promptly after disruption.

In this respect, our results are consistent with the assumption that TDEs undergo a soft-to-hard spectral transition at $\dot{m} \sim 0.03$, phenomenologically resembling scaled-up XRBs in terms of the critical Eddington ratio. Recent studies found that TDEs with coronae are more X-ray variable than thermal TDEs, typically at the >10 per cent level on 1–10 ks time-scales (J. Chakraborty et al. 2026), which is compatible with our observations of AT2024lhc and AT2024kmq. This further supports a scenario in which corona formation enhances variability, again reminiscent of XRB behaviour. However, the characteristic time-scales of these transitions differ markedly: XRB state changes typically occur over hours to a few days, whereas the analogous transitions inferred in TDEs occur over a few to tens of days (T. Wevers et al. 2021; Y. Yao et al. 2022), corresponding to much shorter durations when expressed in units of the BH dynamical or viscous time-scales. The physical origin of this discrepancy remains unclear (but see possible explanations by H. Noda & C. Done 2018) and warrants further investigation in future theoretical work.

4.2.2 *A note on radio observations*

In the context of XRBs, the soft-to-hard state transition is also associated with mass ejection and radio emission from a compact jet (R. P. Fender et al. 2004), and the 5 GHz radio luminosity L_R, the 2–10 keV X-ray luminosity, and BH mass are observed to follow the 'Fundamental Plane (FP) of black hole activity' (E. Gallo, R. P. Fender & G. G. Pooley 2003; A. Merloni, S. Heinz & T. di Matteo 2003; H. Falcke, E. Körding & S. Markoff 2004). It has been shown that some TDEs may also follow the FP (J. M. Mïller & K. Gültekin 2011; D. R. Pasham & S. van Velzen 2018; K. D. Alexander et al. 2026). We use this empirical relation to predict the expected radio emission from our TDEs and compare it to our observations.

For AT2024kmq at $t_{obs} = 232$ d, the 2–10 keV X-ray luminosity is $\log L_X = 43.90 \pm 0.17$. Using the FP relation from K. Gültekin et al. (2019) and taking the σ_*-inferred BH mass (Table 1), the radio luminosity should be $\log L_R = 39.88^{+0.72}_{-0.69}$, which exceeds the observed radio upper limit (Section 3.5) by 1.3σ. Similarly, for AT2024lhc at $t_{obs} = 77$ d, we have $\log L_X = 43.98^{+0.24}_{-0.25}$ and expect $\log L_R = 40.34^{+0.75}_{-0.70}$, which is more luminous than the transient radio upper limit by 3.1σ. The tension with the FP predictions suggests either intrinsically weak/absent outflows or an off-axis jet geometry. Further radio monitoring is warranted to confirm

or rule out delayed jet brightening expected from off-axis configurations.

We note that the launch of a radio-emitting jet or outflow at $\dot{m} \sim 0.03$ is one of the scenarios proposed by D. Giannios & B. D. Metzger (2011) for TDEs in the soft-to-hard transition regime. K. D. Alexander et al. (2026) recently attempted to test this scenario and found suggestive evidence; however, their estimates of the mass accretion rate, based on the MOSFIT framework, are subject to significant systematic uncertainties (especially at late times). Interestingly, the only X-ray-detected TDE in their sample that is radio underluminous relative to the FP at $t < 1$ yr is AT2018fyk, which also has the highest BH mass of any TDE in their sample [$\log(M_{\rm BH}/{\rm M}_\odot) = 8.0 \pm 0.3$; T. Wevers 2020; K. D. Alexander et al. 2026]. AT2018fyk underwent a clear soft-to-hard transition at $\sim 100-200$ d (T. Wevers et al. 2021), but was not detected in the radio until 1991 d post-discovery (Y. Cendes et al. 2024). After its radio detection, AT2018fyk was found to roughly follow the FP (K. D. Alexander et al. 2026). This could suggest either that AT2018fyk's radio emission was indeed powered by a jet launched at the time of the X-ray state transition but was suppressed at earlier times due to relativistic beaming and an off-axis viewing angle, or that its radio-emitting jet or outflow was not launched until well after this transition occurred. This example also motivates long-term radio monitoring of AT2024kmq and AT2024lhc to search for analogous behaviour.

4.3 Optical precursor from self-intersecting shocks

AT2024kmq exhibited a red ($T_{\rm bb} \sim 6 \times 10^3$ K) and rapidly fading (duration ~ 10 d, Fig. 3) precursor outburst that preceded the main optical peak by ~ 30 d (rest frame). A. Y. Q. Ho et al. (2025) proposed two scenarios for this early emission: (1) an optically thin synchrotron component powered by a forward shock driven by a jet, analogous to GRB afterglows (T. Matsumoto & B. D. Metzger 2023), or (2) expanding debris generated by self-intersection of the stellar streams, where a fraction of the stream kinetic energy is converted to thermal energy. Scenario (1) predicts a rising late-time radio light curve; our non-detection of bright radio emission out to $t_{\rm rest} \sim 1$ yr (Fig. 8) disfavours this interpretation for AT2024kmq.

The self-intersection scenario provides a natural explanation for the precursor emission. For the massive BH powering AT2024kmq ($M_{\rm BH} \sim 10^8\,{\rm M}_\odot$), the collision between incoming and outgoing debris streams (expected to facilitate circularization and disc formation) occurs at $\lesssim 10 r_{\rm g}$ for canonical impact parameters, even for partial disruptions. The relative velocity between the streams at the moment of self-intersection therefore amounts to tens of per cent of the speed of light, leading to substantial kinetic energy dissipation and heating of the gas (i.e. the strong nature of the shock implies the downstream gas is radiation-dominated, reaching radiation and gas temperatures on the order of $\sim 10^6$ K). In such scenarios, radiation-hydrodynamical simulations (Y.-F. Jiang, Guillochon & Loeb 2016; X. Huang, S. W. Davis & Y.-f. Jiang 2023, 2024), as well as analytical estimates (L. Dai, J. C. McKinney & M. C. Miller 2015; W. Lu & C. Bonnerot 2020; C. Bonnerot, W. Lu & P. F. Hopkins 2021), suggest that some of the debris can be ejected from the system at substantial fractions of the self-intersection speed. If this self-intersection creates an expanding cloud of debris (also seen in radiation-hydrodynamical simulations; Y.-F. Jiang et al. 2016), then A. Y. Q. Ho et al. (2025) found that many properties of the precursor exhibited by AT2024kmq, including its temperature, duration, and overall energetics, could be explained by the emission from this byproduct of the self-intersection.

AT2024lhc exhibited qualitatively similar behaviour, with a luminous, rapidly fading precursor and comparable BH mass (Figs 3, 9), supporting a similar physical origin. The precursor in AT2024lhc has a higher effective temperature ($T_{\rm bb} \sim 2 \times 10^4$ K, a factor of ~ 3 larger than AT2024kmq), which remains consistent with the simulations of Y.-F. Jiang et al. (2016) and likely reflects a smaller photospheric radius (and correspondingly higher temperature) when the expanding debris was first detected.

The self-intersection paradigm applies to TDEs across the BH mass spectrum, raising the question: why are such precursors rare? As suggested by A. Y. Q. Ho et al. (2025), lower-mass BHs ($M_{\rm BH} \lesssim 10^7{\rm M}_\odot$) have larger self-intersection radii where dissipation is less efficient, producing weaker or absent optical signatures. At these radii, more debris remains bound, with radiation advected inward rather than emitted by outward-propagating material. Since the volumetric rate of TDEs peaks at lower BH masses (Y. Yao et al. 2023), the same phenomenon may be ubiquitous but simply more difficult to detect in the dominant TDE population.

4.4 Post-precursor UV/optical emission

4.4.1 Power sources of the main peak

The origin of the peak UV/optical emission in TDEs remains actively debated. Available TDE models that produce UV/optical light curves, such as the TDE module in MOSFIT (B. Mockler, J. Guillochon & E. Ramirez-Ruiz 2019), the reprocessing-outflow model of T. Matsumoto & T. Piran (2021), and the quasi-spherical cooling envelope model in REDBACK (N. Sarin & B. D. Metzger 2024), when applied to TDEs with $M_{\rm BH} > 10^7{\rm M}_\odot$ (inferred from host galaxies), systematically underestimate BH masses (P. Ramsden et al. 2022; E. Hammerstein et al. 2023a; J. L. Wise et al. 2026; M. Guolo et al. 2025), suggesting missing physics in the models or alternative emission mechanisms.

The large BH mass inferred for AT2024kmq and AT2024lhc facilitates prompt self-intersection and ensuing accretion, and the fact that standard accretion disc theory successfully explains the observed X-ray state transitions (Section 4.2) strongly supports accretion as the dominant power source. Indeed, during the entire X-ray monitoring phase of AT2024lhc ($t_{\rm rest} \geq 48$ d) and at later times in AT2024kmq ($t_{\rm rest} \gtrsim 100$ d), the X-ray light curves roughly track the UV/optical decline: both decline by about one order of magnitude over ~ 1 yr (Figs 1, 2, and 9). Since the coronal X-ray emission is powered by Comptonization of disc photons, the observed correlation between X-ray and UV/optical luminosities suggests that both trace the disc accretion rate.

We can test whether accretion power alone accounts for the UV/optical luminosity by comparing the peak bolometric luminosity to the expected accretion luminosity at the state transition threshold. Under the assumptions of Section 4.2, if accretion is the sole power source, we expect $\lambda_{\rm Edd,peak} \lesssim 0.03$ at the optical peak. This prediction is consistent with observations of AT2024lhc (Table 3). However, AT2024kmq reaches $\lambda_{\rm Edd,peak} \gtrsim 0.04$, suggesting that there is likely an additional power source (at least at its UV/optical peak), most likely shocks from stream–disc collisions (E. Steinberg & N. C. Stone 2024) and circularization shocks within the accretion flow (X. Huang et al. 2025).

4.4.2 *AT2024kmq's late-time rebrightening*

Late-time rebrightening has been observed in numerous TDEs. They exhibit diverse characteristics in timing, luminosity, and light curve morphology. Some events show significant, multiple undulations during the decline phase (T. Wevers et al. 2021; Y. Yao et al. 2025), while others exhibit discrete flares with shapes and amplitudes either similar (A. V. Payne et al. 2021; Z. Lin et al. 2024; J. J. Somalwar et al. 2025; C. R. Angus et al. 2026) or markedly different (E. Kankare et al. 2017; A. Malyali et al. 2021; Y. Yao et al. 2023) from the initial outburst. When well-separated flares display similar characteristics, they are commonly interpreted as repeated partial TDEs from a single star on an eccentric orbit (C. Liu, R. Yarza & E. Ramirez-Ruiz 2025; S. Zhong 2025) or as distinct TDEs from multiple stars (I. Mandel & Y. Levin 2015).

For AT2024kmq, the modest amplitude of the rebrightening favors a single TDE with multiphase evolution rather than a repeated disruption scenario. Several physical mechanisms have been proposed to explain such rebrightenings. Some models attribute the initial flare to shock-powered emission and the subsequent rebrightening to delayed accretion disc formation (J.-H. Chen, L.-M. Dou & R.-F. Shen 2022; H. Guo et al. 2025), while others invoke interactions between disc winds or debris streams and a dusty torus (N. Jiang et al. 2019; J. Zhuang & R.-F. Shen 2021) – a scenario particularly relevant for TDEs in radiative-mode AGNs.

In the case of AT2024kmq, multiple lines of evidence point to early disc formation (Section 4.2), ruling out delayed accretion as the origin of the rebrightening. Furthermore, the WISE colour (Table 1) argues against the presence of a dusty torus, disfavouring wind–torus interaction scenarios. Given that the host galaxy harbours a jet-mode AGN, which likely possesses a truncated thin disc (Section 3.5.2), we speculate that the rebrightening arises from interactions between TDE's newly formed accretion flow and the pre-existing truncated accretion flow. Future theoretical work exploring TDE-truncated disc interactions may naturally explain the late-time rebrightenings observed in TDEs hosted by radio-loud AGNs.

5 CONCLUSION

We have presented multiwavelength observations of two luminous featureless TDEs, AT2024kmq and AT2024lhc. Both events are hosted by MBHs ($M_{\rm BH} \sim 10^8 {\rm M}_\odot$) and share distinctive observational signatures.

They exhibit luminous ($L_{\rm X,peak} \sim 10^{44}$ erg s^{-1}), rapidly variable (minimum observed time-scale $\sim$ 1.2–4.8 h) X-ray emission appearing at early times ($t_{\rm rest} < 50$ d, contemporaneous with or preceding the optical peak). Their X-ray spectra are characterized by power-law photon indices $1.7 < \Gamma < 3$, with NuSTAR detecting photons extending to $\sim$20 keV. Rapid variability restricts the X-ray emitting region to $R_{\rm X} \lesssim 10 r_{\rm g}$, while the absence of radio emission disfavors relativistic jets. We interpret this emission as inverse Compton scattering in a compact corona, formed within $\sim$ 50 d of disruption, far more rapidly than the $\sim$200–1000 d time-scales observed in lower-mass ($M_{\rm BH} \sim 10^6$–$10^7 {\rm M}_\odot$) TDE systems (Y. Yao et al. 2022; A. Hajela et al. 2025).

For TDEs as a population, we find that the various X-ray spectral states observed can be understood with simple disc theory, assuming that soft-to-hard state transition happens at a time when the Eddington-normalized mass accretion rate declines to the critical value of $\dot{m} \sim 0.03$ (Section 4.2.1). This observational result confirms the theoretical prediction of A. Mummery & S. A. Balbus (2021b). From the perspective of X-ray state transitions, the accretion discs of TDEs behave phenomenologically as scaled-up versions of XRBs, although the fast duration of the transition and the radio non-detections warrant further investigation.

Both AT2024kmq and AT2024lhc also exhibited optical precursor outbursts that preceded the main peak by $\sim$30 d (rest frame), and are consistent with being powered by shocks generated by debris stream self-intersection. If this interpretation is correct, optical precursors should be more prominent in TDEs around more MBHs – a prediction that can be tested with future systematic searches and analyses of TDE precursor emission.

Through systematic comparison of 49 ZTF TDEs spanning four spectral sub-types (TDE-H + He, TDE-H, TDE-He, and TDE-featureless), we find that featureless TDEs are hosted by high-mass BHs, consistent with the findings of E. Hammerstein et al. (2023a). Featureless TDEs exhibit robust bimodality in both peak blackbody luminosity and radius. AT2024kmq and AT2024lhc belong to the high-luminosity, large-radius sub-class. These two sub-classes likely represent two ways (i.e. high source luminosity and small photosphere; Fig. 12) to achieve the high ionization required to suppress spectral lines as demonstrated in O. Aspegren & D. Kasen (2026).

ACKNOWLEDGEMENTS

YY, RC, and EH acknowledge support from the NASA/NuSTAR GO programme, grant 80NSSC25K7488. AM acknowledges support from the Ambrose Monell Foundation, the W. M. Keck Foundation and the John N. Bahcall Fellowship Fund at the Institute for Advanced Study. MG acknowledges support by the Ministry of Science and Higher Education grant 075-15-2024-647. ERC acknowledges support from the National Aeronautics and Space Administration through the Astrophysics Theory Program, grant 80NSSC24K0897. DRP acknowledges the support of the NASA/NuSTAR GO programme, grant 80NSSC25K7949. KDA gratefully acknowledges support provided by the NSF through award AST-2307668 and from the Alfred P. Sloan Foundation. CRA, MN, and XS are supported by the European Research Council (ERC) under the European Union's Horizon 2020 research and innovation programme (grant agreement No. 948381). MWC acknowledges support from the National Science Foundation with grant numbers PHY-2117997, PHY-2308862, and PHY-2409481.

This work is partly based on observations with the NASA/ESA *Hubble Space Telescope* obtained at the Space Telescope Science Institute, which is operated by the Association of Universities for Research in Astronomy, Incorporated, under NASA contract NAS5-26555. Support for Program number GO-17667 was provided through a grant from the STScI under NASA contract NAS5-26555.

Based on observations obtained with the Samuel Oschin Telescope 48-inch and the 60-inch Telescope at the Palomar Observatory as part of the Zwicky Transient Facility project. ZTF is supported by the National Science Foundation under Grant Nos AST-1440341, AST-2034437, and currently Award #2407588. ZTF receives additional funding from the ZTF partnership. Cur-

rent members include Caltech, USA; Caltech/IPAC, USA; University of Maryland, USA; University of California, Berkeley, USA; University of Wisconsin at Milwaukee, USA; Cornell University, USA; Drexel University, USA; University of North Carolina at Chapel Hill, USA; Institute of Science and Technology, Austria; National Central University, Taiwan, and OKC, University of Stockholm, Sweden. Operations are conducted by Caltech's Optical Observatory (COO), Caltech/IPAC, and the University of Washington at Seattle, USA.

The Gordon and Betty Moore Foundation, through both the Data-Driven Investigator Program and a dedicated grant, provided critical funding for SkyPortal. The ZTF forced-photometry service was funded under the Heising-Simons Foundation grant No. 12540303 (PI: Graham).

The National Radio Astronomy Observatory is a facility of the National Science Foundation operated under cooperative agreement by Associated Universities, Inc.

This work has made use of data from the Asteroid Terrestrial-impact Last Alert System (ATLAS) project. The ATLAS project is primarily funded to search for near earth asteroids through NASA grants NN12AR55G, 80NSSC18K0284, and 80NSSC18K1575; byproducts of the NEO search include images and catalogues from the survey area. This work was partially funded by Kepler/K2 grant J1944/80NSSC19K0112 and *HST* GO-15889, and STFC grants ST/T000198/1 and ST/S006109/1. The ATLAS science products have been made possible through the contributions of the University of Hawaii Institute for Astronomy, the Queen's University Belfast, the Space Telescope Science Institute, the South African Astronomical Observatory, and The Millennium Institute of Astrophysics (MAS), Chile.

This work uses data obtained with eROSITA telescope onboard *SRG* observatory. The *SRG* observatory was built by Roskosmos with the participation of the Deutsches Zentrum für Luft- und Raumfahrt (DLR). The SRG/eROSITA X-ray telescope was built by a consortium of German Institutes led by MPE, and supported by DLR. The *SRG* spacecraft was designed, built, launched and is operated by the Lavochkin Association and its sub-contractors. The science data were downlinked via the Deep Space Network Antennae in Bear Lakes, Ussurijsk, and Baykonur, funded by Roskosmos. The eROSITA data used in this work were processed using the eSASS software system developed by the German eROSITA consortium and proprietary data reduction and analysis software developed by the Russian eROSITA Consortium.

Some of the data presented herein were obtained at Keck Observatory, which is a private 501(c)3 non-profit organization operated as a scientific partnership among the California Institute of Technology, the University of California, and the National Aeronautics and Space Administration. The Observatory was made possible by the generous financial support of the W. M. Keck Foundation. The authors wish to recognize and acknowledge the very significant cultural role and reverence that the summit of Maunakea has always had within the Native Hawaiian community. We are most fortunate to have the opportunity to conduct observations from this mountain.

A major upgrade of the Kast spectrograph on the Shane 3 m telescope at Lick Observatory, led by Brad Holden, was made possible through gifts from the Heising-Simons Foundation, William and Marina Kast, and the University of California Observatories. Research at Lick Observatory is partially supported by a generous gift from Google.

Based on observations made with the Liverpool Telescope operated on the island of La Palma by Liverpool John Moores University in the Spanish Observatorio del Roque de los Muchachos of the Instituto de Astrofisica de Canarias with financial support from the UK Science and Technology Facilities Council.

Partly based on observations made with the Nordic Optical Telescope, owned in collaboration by the University of Turku and Aarhus University at the Observatorio del Roque de los Muchachos, La Palma, Spain, of the Instituto de Astrofisica de Canarias. The NOT data were obtained under programme ID P68-501.

This research has made use of data from the NuSTAR mission, a project led by the California Institute of Technology, managed by the Jet Propulsion Laboratory, and funded by the National Aeronautics and Space Administration. Data analysis was performed using the NuSTAR Data Analysis Software (NUSTARDAS), jointly developed by the ASI Science Data Center (SSDC, Italy) and the California Institute of Technology (USA).

DATA AVAILABILITY

The data behind Figs 1–5 are available at https://github.com/yaoyuhan/TDE-2024lhc-2024kmq/. Other data underlying this article that are not in the Appendix will be shared on reasonable request to the corresponding author.

REFERENCES

Ahumada R. et al., 2020, ApJS, 249, 3
Albareti F. D. et al., 2017, ApJS, 233, 25
Alexander K. D. et al., 2026, ApJ, 1000, 139
Alush Y., Stone N. C., van Velzen S., 2025, preprint (arXiv:2510.24696)
Andreoni I. et al., 2022, Nature, 612, 430
Angus C. R. et al., 2026, preprint (arXiv:2601.04406)
Aspegren O., Kasen D., 2026, ApJ, 1001, 191
Auchettl K., Guillochon J., Ramirez-Ruiz E., 2017, ApJ, 838, 149
Bardeen J. M., Press W. H., Teukolsky S. A., 1972, ApJ, 178, 347
Bellm E. C. et al., 2019, PASP, 131, 018002
Belloni T. M., 2010, in Belloni T., ed., Vol. 794, The Jet Paradigm. Springer, Berlin, p. 53
Beloborodov A. M., Illarionov A. F., Ivanov P. B., Polnarev A. G., 1992, MNRAS, 259, 209
Beniamini P., Piran T., Matsumoto T., 2023, MNRAS, 524, 1386
Berger V., Kara E., Chakraborty J., Masterson M., Burdge K., 2026, ApJ, 999, 265
Blandford R. D., Payne D. G., 1981, MNRAS, 194, 1033
Bonnerot C., Lu W., Hopkins P. F., 2021, MNRAS, 504, 4885
Brightman M. et al., 2021, ApJ, 909, 102
Burrows D. N. et al., 2005, Space Sci. Rev., 120, 165
Calzetti D., Armus L., Bohlin R. C., Kinney A. L., Koornneef J., Storchi-Bergmann T., 2000, ApJ, 533, 682
Cappellari M., 2023, MNRAS, 526, 3273
Cardelli J. A., Clayton G. C., Mathis J. S., 1989, ApJ, 345, 245
CASA Team, 2022, PASP, 134, 114501
Cash W., 1979, ApJ, 228, 939
Cendes Y., Berger E., Alexander K., Laskar T., Goodwin A., 2024, Astron. Telegram, 16650, 1
Cenko S. B. et al., 2016, ApJ, 818, L32
Chakraborty J. et al., 2024, ApJ, 965, 12
Chakraborty J., Masterson M., Mummery A., Kara E., Panagiotou C., Arcodia R., Berger V., 2026, ApJ, 1000, 95
Chambers K. C. et al., 2016, preprint (arXiv:1612.05560)
Charalampopoulos P. et al., 2022, A&A, 659, A34
Chen J.-H., Dou L.-M., Shen R.-F., 2022, ApJ, 928, 63

Chornock R., 2024, Transient Name Server Classification Report, 2024-2237, 1
Condon J. J., Cotton W. D., Broderick J. J., 2002, AJ, 124, 675
Conroy C., Gunn J. E., White M., 2009, ApJ, 699, 486
Coughlin E. R., Nixon C. J., 2022, ApJ, 936, 70
Coughlin M. W. et al., 2023, ApJS, 267, 31
D'Orazio D. J., Loeb A., Guillochon J., 2019, MNRAS, 485, 4413
Dai L., McKinney J. C., Miller M. C., 2015, ApJ, 812, L39
Debes J. et al., 2024, The Hubble Advanced Spectral Product (HASP) Program, Instrument Science Report COS 2024-01. p. 31
Dekany R. et al., 2020, PASP, 132, 038001
DESI Collaboration, 2022, AJ, 164, 207
DESI Collaboration, 2026, AJ, 171, 285
Done C., Gierliński M., Kubota A., 2007, A&AR, 15, 1
Du P., Egaña-Ugrinovic D., Essig R., Fragione G., Perna R., 2022, Nat. Commun., 13, 4626
Dunn R. J. H., Fender R. P., Körding E. G., Belloni T., Cabanac C., 2010, MNRAS, 403, 61
Eftekhari T. et al., 2024, ApJ, 974, 149
Fabian A. C., 2016, Astronomische Nachrichten, 337, 375
Falcke H., Körding E., Markoff S., 2004, A&A, 414, 895
Fender R. P., Belloni T. M., Gallo E., 2004, MNRAS, 355, 1105
Foreman-Mackey D., Hogg D. W., Lang D., Goodman J., 2013, PASP, 125, 306
Frederick S. et al., 2021, ApJ, 920, 56
Fremling C. et al., 2016, A&A, 593, A68
Fruscione A. et al., 2006, in Silva D. R., Doxsey R. E., eds, Proc. SPIE Conf. Ser. Vol. 6270, Observatory Operations: Strategies, Processes, and Systems. SPIE, Bellingham, p. 62701V
Gabriel C. et al., 2004, in Ochsenbein F., Allen M. G., Egret D., eds, ASP Conf. Ser. Vol. 314, Astronomical Data Analysis Software and Systems (ADASS) XIII. Astron. Soc. Pac., San Francisco, p. 759
Gallo E., Fender R. P., Pooley G. G., 2003, MNRAS, 344, 60
Garmire G. P., Bautz M. W., Ford P. G., Nousek J. A., Ricker George R. J., 2003, in Truemper J. E., Tananbaum H. D., eds, Proc. SPIE Conf. Ser. Vol. 4851, X-Ray and Gamma-Ray Telescopes and Instruments for Astronomy. SPIE, Bellingham, p. 28
Gendreau K. C. et al., 2016, in Space Telescopes and Instrumentation 2016: Ultraviolet to Gamma Ray. p. 99051H
Giannios D., Metzger B. D., 2011, MNRAS, 416, 2102
Gilfanov M., 2010, in Belloni T., ed., Vol. 794, The Jet Paradigm. Springer, Berlin, p. 17
Gilfanov M., Merloni A., 2014, Space Sci. Rev., 183, 121
Graham M. J. et al., 2019, PASP, 131, 078001
Gültekin K., King A. L., Cackett E. M., Nyland K., Miller J. M., Di Matteo T., Markoff S., Rupen M. P., 2019, ApJ, 871, 80
Gunn J. E. et al., 2006, AJ, 131, 2332
Guo H. et al., 2025, ApJ, 979, 235
Guolo M., Gezari S., Yao Y., van Velzen S., Hammerstein E., Cenko S. B., Tokayer Y. M., 2024, ApJ, 966, 160
Guolo M. et al., 2025, preprint (arXiv:2510.26774)
Hajela A. et al., 2025, ApJ, 983, 29
Hammerstein E. et al., 2023a, ApJ, 942, 9
Hammerstein E. et al., 2023b, ApJ, 957, 86
Hammerstein E. et al., 2026, ApJ, 996, 143
Harrison F. A. et al., 2013, ApJ, 770, 103
Heckman T. M., Best P. N., 2014, ARA&A, 52, 589
Heckman T. M., Kauffmann G., Brinchmann J., Charlot S., Tremonti C., White S. D. M., 2004, ApJ, 613, 109
Hills J. G., 1975, Nature, 254, 295
Hinkle J. T., 2024, MNRAS, 531, 2603
Hinkle J. T. et al., 2022, ApJ, 930, 12
Ho A. Y. Q. et al., 2025, ApJ, 989, 54
Huang H.-T., Lu W., 2024, MNRAS, 527, 1865
Huang X., Davis S. W., Jiang Y.-f., 2023, ApJ, 953, 117
Huang X., Davis S. W., Jiang Y.-f., 2024, ApJ, 974, 165
Huang X., Meza M. R., Yun S. B., Mockler B., Davis S. W., Jiang Y.-f., 2025, preprint (arXiv:2512.12985)
Hung T. et al., 2021, ApJ, 917, 9
Ivezić Ž. et al., 2019, ApJ, 873, 111
Jiang Y.-F., Guillochon J., Loeb A., 2016, ApJ, 830, 125
Jiang N., Wang T., Mou G., Liu H., Dou L., Sheng Z., Wang Y., 2019, ApJ, 871, 15
Jiang Y.-F., Blaes O., Kaul I., Zhang L., 2025, ApJ, 988, 43
Johnson B. D., Leja J., Conroy C., Speagle J. S., 2021, ApJS, 254, 22
Jonker P. G., Stone N. C., Generozov A., van Velzen S., Metzger B., 2020, ApJ, 889, 166
Kaastra J. S., Bleeker J. A. M., 2016, A&A, 587, A151
Kankare E. et al., 2017, Nat. Astron., 1, 865
Kara E., García J., 2025, ARA&A, 63, 379
Kesden M., 2012, Phys. Rev. D, 85, 024037
King A. R., Pringle J. E., Livio M., 2007, MNRAS, 376, 1740
Komossa S., Bade N., 1999, A&A, 343, 775
Komossa S. et al., 2008, ApJ, 678, L13
Kormendy J., Ho L. C., 2013, ARA&A, 51, 511
Kroupa P., 2001, MNRAS, 322, 231
Lacy J. H., Townes C. H., Hollenbach D. J., 1982, ApJ, 262, 120
Laskar T. et al., 2014, ApJ, 781, 1
Lin Z. et al., 2024, ApJ, 971, L26
Liu C., Yarza R., Ramirez-Ruiz E., 2025, ApJ, 979, 40
Lu W., Bonnerot C., 2020, MNRAS, 492, 686
Maccarone T. J., 2003, A&A, 409, 697
Malyali A. et al., 2021, A&A, 647, A9
Mandel I., Levin Y., 2015, ApJ, 805, L4
Masci F. J. et al., 2019, PASP, 131, 018003
Masci F. J. et al., 2023, preprint (arXiv:2305.16279)
Matsumoto T., Metzger B. D., 2023, MNRAS, 522, 4028
Matsumoto T., Piran T., 2021, MNRAS, 502, 3385
Merloni A., Heinz S., di Matteo T., 2003, MNRAS, 345, 1057
Miller J. M., Gültekin K., 2011, ApJ, 738, L13
Miller J. S., Stone R. P. S., 1993, Lick Observatory Technical Reports, 66
Mockler B., Guillochon J., Ramirez-Ruiz E., 2019, ApJ, 872, 151
Moustakas J., Scholte D., Dey B., Khederlarian A., 2023, Astrophysics Source Code Library, record ascl:2308.005
Mummery A., 2024, MNRAS, 527, 6233
Mummery A., 2026, MNRAS, 547, stag387
Mummery A., Balbus S. A., 2020, MNRAS, 492, 5655
Mummery A., Balbus S. A., 2021a, MNRAS, 504, 4730
Mummery A., Balbus S. A., 2021b, MNRAS, 505, 1629
Mummery A., van Velzen S., Nathan E., Ingram A., Hammerstein E., Fraser-Taliente L., Balbus S., 2024, MNRAS, 527, 2452
Mummery A., Nathan E., Ingram A., Gardner M., 2025a, MNRAS, 544, 2225,
Mummery A., Metzger B., van Velzen S., Guolo M., 2025b, preprint (arXiv:2512.09143)
Nicholl M. et al., 2023, ApJ, 954, L28
Noda H., Done C., 2018, MNRAS, 480, 3898
Oke J. B. et al., 1995, PASP, 107, 375
Onori F. et al., 2022, MNRAS, 517, 76
Pasham D. R., van Velzen S., 2018, ApJ, 856, 1
Payne A. V. et al., 2021, ApJ, 910, 125
Perley R. A., Chandler C. J., Butler B. J., Wrobel J. M., 2011, ApJ, 739, L1
Phinney E. S., 1989, in Morris M., ed., IAU Symposium Vol. 136, The Center of the Galaxy. Kluwer, Dordrecht. p. 543
Predehl P. et al., 2021, A&A, 647, A1
Prochaska J. X. et al., 2020a, pypeit/PypeIt: Release 1.0.0, Zenodo
Prochaska J. X. et al., 2020b, J. Open Source Softw., 5, 2308
Ramsden P., Lanning D., Nicholl M., McGee S. L., 2022, MNRAS, 515, 1146
Rees M. J., 1988, Nature, 333, 523
Remillard R. A., McClintock J. E., 2006, ARA&A, 44, 49
Rest S. et al., 2025, ApJ, 979, 114
Roming P. W. A. et al., 2005, Space Sci. Rev., 120, 95
Sarin N., Metzger B. D., 2024, ApJ, 961, L19
Sazonov S. et al., 2021, MNRAS, 508, 3820
Schlafly E. F., Finkbeiner D. P., 2011, ApJ, 737, 103

Schlafly E. F., Meisner A. M., Green G. M., 2019, ApJS, 240, 30
Sfaradi I. et al., 2024, MNRAS, 527, 7672
Shakura N. I., Sunyaev R. A., 1973, A&A, 24, 337
Shingles L. et al., 2021, Transient Name Server AstroNote, 7, 1
Silverman J. M. et al., 2012, MNRAS, 425, 1789
Simard L., Mendel J. T., Patton D. R., Ellison S. L., McConnachie A. W., 2011, ApJS, 196, 11
Smith K. W. et al., 2020, PASP, 132, 085002
Somalwar J. J. et al., 2025, ApJ, 985, 175
Steele I. A. et al., 2004, in Oschmann Jacobus M. J., ed., Proc. SPIE Conf. Ser. Vol. 5489, Ground-based Telescopes. SPIE, Bellingham, p. 679
Steinberg E., Stone N. C., 2024, Nature, 625, 463
Stern D. et al., 2012, ApJ, 753, 30
Sunyaev R. A., Titarchuk L. G., 1980, A&A, 86, 121
Sunyaev R. et al., 2021, A&A, 656, A132
Tetarenko B. E., Sivakoff G. R., Heinke C. O., Gladstone J. C., 2016, ApJS, 222, 15
Tonry J. L. et al., 2018, PASP, 130, 064505
Vahdat Motlagh A., Kalemci E., Maccarone T. J., 2019, MNRAS, 485, 2744
van der Walt S., Crellin-Quick A., Bloom J., 2019, J. Open Source Softw., 4, 1247
van Velzen S., Stone N. C., Metzger B. D., Gezari S., Brown T. M., Fruchter A. S., 2019, ApJ, 878, 82
van Velzen S., Holoien T. W. S., Onori F., Hung T., Arcavi I., 2020, Space Sci. Rev., 216, 124
van Velzen S. et al., 2021, ApJ, 908, 4
Wang T.-G., Zhou H.-Y., Wang L.-F., Lu H.-L., Xu D., 2011, ApJ, 740, 85
Wang T.-G., Zhou H.-Y., Komossa S., Wang H.-Y., Yuan W., Yang C., 2012, ApJ, 749, 115
Wevers T., 2020, MNRAS, 497, L1
Wevers T. et al., 2021, ApJ, 912, 151
Willingale R., Starling R. L. C., Beardmore A. P., Tanvir N. R., O'Brien P. T., 2013, MNRAS, 431, 394
Wise J. L. et al., 2026, MNRAS, 546, stag130
Wiseman P. et al., 2025, MNRAS, 537, 2024
Woodgate B. E. et al., 1998, PASP, 110, 1183
Yao Y. et al., 2019, ApJ, 886, 152
Yao Y. et al., 2022, ApJ, 937, 8
Yao Y. et al., 2023, ApJ, 955, L6
Yao Y., Chornock R., Guo X., LeBaron N., Margutti R., Ravi V., Somalwar J., 2024a, Transient Name Server AstroNote, 177, 1
Yao Y., Lu W., Harrison F., Kulkarni S. R., Gezari S., Guolo M., Cenko S. B., Ho A. Y. Q., 2024b, ApJ, 965, 39
Yao Y. et al., 2025, ApJ, 993, 198
Yuan F., Narayan R., 2004, ApJ, 612, 724
Yuan F., Narayan R., 2014, ARA&A, 52, 529
Zhang Z. et al., 2026, A&A, 708, A374
Zhong S., 2025, ApJ, 983, 131
Zhu J. et al., 2025, ApJ, 994, L16
Zhuang J., Shen R.-F., 2021, J. High Energy Astrophys., 32, 11

APPENDIX A: SUPPLEMENTARY FIGURES

The results of joint NuSTAR + XRT spectral fitting are shown in Fig. A1.

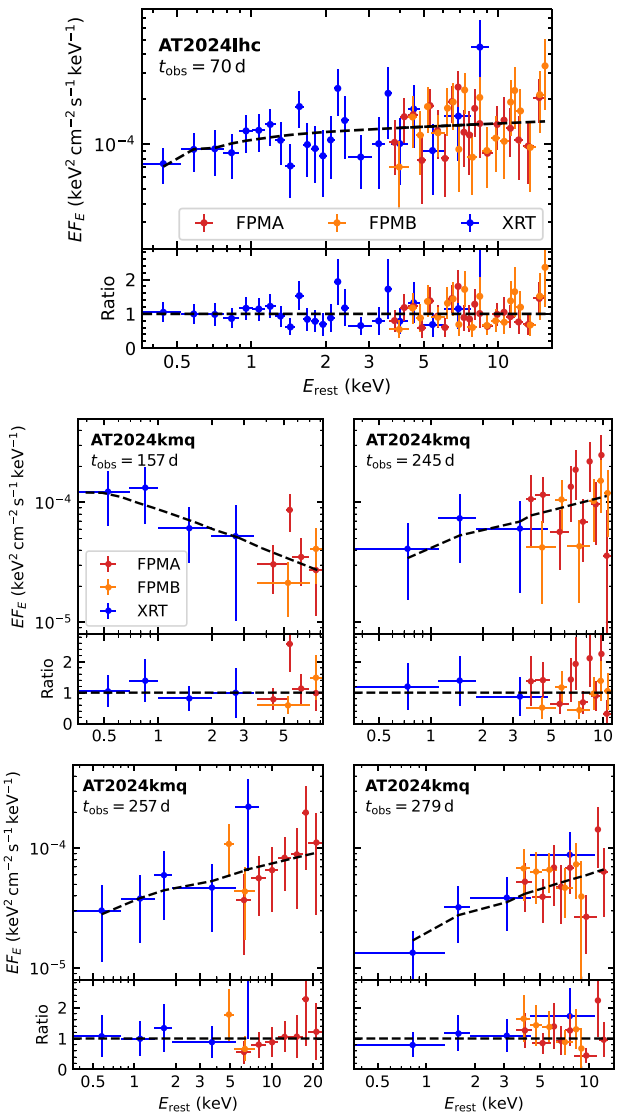

Figure A1. Joint spectral fitting between NuSTAR and XRT. The dashed lines show the best-fitting absorbed power-law model.

APPENDIX B: SUPPLEMENTARY TABLES

A log of optical spectroscopy of AT2024kmq and AT2024lhc is presented in Table B1. A log of NuSTAR observations is presented in Table B2. A log of *XMM–Newton* and *Chandra* observations is presented in Table B3. The VLA observation logs are presented in Tables B4–B5.

Table B1. Log of optical spectroscopy.

IAU name	Start date (UT)	$t_{\rm rest}$ (d)	Telescope	Instrument	Wavelength range (Å)	Slit width (arcsec)	Exp. (s)
AT2024lhc	2024-06-14.4	42	Shane	Kast	3525–10500	2.0	3660/3600 [a]
AT2024lhc	2024-06-28.3	54	Shane	Kast	3525–10500	2.0	3660/3600 [a]
AT2024lhc	2024-07-02.5	57	Keck I	LRIS	3260–10250	1.0	650/600 [a]
AT2024lhc	2024-07-29.4	80	Keck I	LRIS	3260–10250	0.7	600
AT2024lhc	2024-08-15.4	94	Shane	Kast	3525–10500	2.0	3660/3600 [a]
AT2024lhc	2024-08-28.4	104	Shane	Kast	3525–10500	2.0	3660/3600 [a]
AT2024lhc	2025-03-05.6	262	Keck I	LRIS	3260–10250	1.0	1200/1150 [a]
AT2024lhc	2026-06-01.5	335	Keck I	LRIS	3260–10250	1.0	2400/2300 [a]
AT2024kmq	2024-11-28.5 [b]	153	Shane	Kast	4170–6830	1.5	3566
AT2024kmq	2024-11-29.5 [b]	154	Shane	Kast	4170–6830	1.5	2145
AT2024kmq	2024-12-08.2	161	NOT	ALFOSC	3500–9700	1.0	3000
AT2024kmq	2025-06-25.6	328	Keck I	LRIS	3260–10250	1.0	2400/2300[a]

Note.[a] Exposure times on blue/red sides of the spectrograph. [b] The red side of Kast was not available on those dates. As such, the 452/3306 grism was used on the blue side to increase the wavelength coverage. These two spectra are combined and displayed as a single spectrum in Fig. 4.

Table B2. NuSTAR observation log and joint spectral fitting with XRT.

Name	obsID	Exp. (ks)	Start time (UT)	$t_{\rm obs}$ (d)	$t_{\rm rest}$ (d)	FPMA count rate (count s^{-1})	Γ	$f_{\rm X}$ (10^{-13} erg s^{-1} cm^{-2})	cstat/dof
AT2024kmq	81001608002 [a]	67.3	2024-11-02.1	157	132	0.0008 ± 0.0002	$2.59^{+0.17}_{-0.18}$	$3.68^{+0.87}_{-0.66}$	31.15/33
	81002638002 [b]	23.0	2025-01-29.5	245	206	0.0026 ± 0.0004	$1.63^{+0.20}_{-0.22}$	$3.66^{+0.61}_{-0.63}$	47.68/39
	81002638004 [b]	22.5	2025-02-10.9	257	216	0.0015 ± 0.0004	$1.72^{+0.16}_{-0.17}$	$2.75^{+0.51}_{-0.39}$	28.09/47
	81002638006 [b]	49.4	2025-03-04.6	279	234	0.0012 ± 0.0002	$1.59^{+0.16}_{-0.18}$	$1.91^{+0.20}_{-0.46}$	45.25/50
AT2024lhc	81001628002 [c]	54.6	2024-07-03.1	70	59	0.0037 ± 0.0003	1.93 ± 0.05	$6.46^{+0.42}_{-0.39}$	81.22/93

Note. The FPMA net count rate is given in the 3–15 keV energy band. $f_{\rm X}$ is the observed 0.3–10 keV X-ray flux. [a] PI: Guolo. Jointly modelled with XRT obsID 16717008. [b] PI: Pasham. The $t_{\rm obs} = 245$ d observation was jointly modeled with XRT obsID 16717015; the $t_{\rm obs} = 279$ d observation was jointly modelled with XRT obsIDs 16717020, 16717016, 16717022; and the $t_{\rm obs} = 257$ d observation was jointly modelled with XRT obsIDs 16717023, 16717024, 16717025. [c] PI: Yao. Jointly modelled with XRT obsID 16665006.

Table B3. XMM-Newton and Chandra observation log and spectral fitting results.

Name	Telescope	obsID	Exp.	Start time	$t_{\rm obs}$	Γ	$f_{\rm X}$	cstat/dof
			(ks)	(UT)	(d)		(10^{-13} erg s^{-1} cm^{-2})	
AT2024kmq	*Chandra*[a]	30886	16.7	2025-05-05.3	340	1.77 ± 0.27	$0.99^{+0.11}_{-0.13}$	32.43/31
AT2024lhc	*XMM–Newton*[b]	0942540201	14.7	2024-09-23.4	152	2.13 ± 0.06	$4.39^{+0.22}_{-0.23}$	30.42/26
	Chandra[a]	30885	15.9	2025-05-06.6	377	1.74 ± 0.15	$3.05^{+0.20}_{-0.17}$	43.28/47
	XMM–Newton[c]	0953000101	7.6	2025-08-14.4	477	$2.06^{+0.30}_{-0.29}$	$0.67^{+0.26}_{-0.12}$	14.84/10

Note. $f_{\rm X}$ is the observed 0.3–10 keV X-ray flux. [a] PI: Yao. Observed as part of the joint VLA + *Chandra* programme 25A-15. [b] PI: Guolo. Observed as part of a dedicated X-ray follow-up programme targeting optically selected TDEs. [c] PI: Chornock. Observed as part of a joint *HST* + *XMM–Newton* programme.

Table B4. Targeted VLA observations of AT2024lhc.

Date	$t_{\rm obs}$ (day)	$t_{\rm rest}$ (day)	Receiver (GHz)	ν_0 (μJy)	f_ν	Array config.
2024-07-10.0	77	64	X	10.0	< 11.4	B
2024-08-25.8	123	102	X	10.0	< 10.2	B
2024-10-22.7	182	151	X	10.0	< 10.5	A
2025-01-17.4	269	222	X	10.0	< 11.4	A
2025-05-26.2	397	329	X	10.0	< 7.5	C
2025-06-02.1	404	335	C	6.0	< 14.4	C

Table B5. Targeted VLA observations of AT2024kmq.

Date	$t_{\rm obs}$ (day)	$t_{\rm rest}$ (day)	Receiver	ν_0 (GHz)	Beam size (arcsec)	Integrated f_ν (μJy)	Peak f_ν (μJy)	Array config.
2025-01-17.6	232	195	X	10.0	0.22×0.20	117 ± 12	66 ± 5	A
2025-01-17.6	232	195	C	6.0	0.42×0.36	156 ± 11	99 ± 5	A
2025-02-27.4	273	229	X	10.0	9.14×7.80	312 ± 19	169 ± 7	D
2025-02-27.4	273	229	C	6.0	15.98×12.53	508 ± 30	340 ± 13	D
2025-03-20.4	294	247	Ku	15.1	5.73×5.56	230 ± 17	130 ± 7	D
2025-03-20.4	294	247	K	22.1	4.53×3.43	173 ± 17	94 ± 6	D
2025-07-02.1	398	334	Ku	15.1	1.85×1.65	158 ± 17	115 ± 8	C
2025-07-02.2	398	334	K	22.0	1.59×1.11	152 ± 14	120 ± 7	C
2025-07-15.1	411	345	X	10.0	2.57×2.46	318 ± 28	165 ± 10	C
2025-07-15.1	411	345	C	6.0	4.52×4.01	561 ± 56	161 ± 13	C

[1]*Miller Institute for Basic Research in Science, 206B Stanley Hall, Berkeley, CA 94720, USA*
[2]*Department of Astronomy, University of California, Berkeley, CA 94720-3411, USA*
[3]*Berkeley Center for Multi-messenger Research on Astrophysical Transients and Outreach (Multi-RAPTOR), University of California, Berkeley, CA 94720-3411, USA*
[4]*School of Natural Sciences, Institute for Advanced Study, 1 Einstein Drive, Princeton, NJ 08540, USA*
[5]*Department of Physics, University of California, 366 Physics North MC 7300, Berkeley, CA 94720, USA*
[6]*Space Research Institute (IKI), Russian Academy of Sciences, Profsoyuznaya 84/32, Moscow 117997, Russia*
[7]*Max-Planck-Institut für Astrophysik, Karl-Schwarzschild-Str 1, D-85741 Garching, Germany*
[8]*Bloomberg Center for Physics and Astronomy, Johns Hopkins University, 3400 N. Charles St., Baltimore, MD 21218, USA*
[9]*Department of Physics, Syracuse University, Syracuse, NY 13210, USA*
[10]*Theoretical Astrophysics Center, University of California, Berkeley, CA 94720, USA*
[11]*Department of Physics & Kavli Institute for Astrophysics and Space Research, Massachusetts Institute of Technology, Cambridge, MA 02139, USA*
[12]*Eureka Scientific, 2452 Delmer Street Suite 100, Oakland, CA 94602, USA*
[13]*Department of Physics, The George Washington University, Washington, DC 20052, USA*
[14]*Department of Astronomy/Steward Observatory, 933 North Cherry Avenue, Room N204, Tucson, AZ 85721-0065, USA*
[15]*Astrophysics Research Centre, School of Mathematics and Physics, Queen's University Belfast, Belfast BT7 1NN, UK*
[16]*Center for Astrophysics | Harvard & Smithsonian, 60 Garden Street, Cambridge, MA 02138-1516, USA*
[17]*McWilliams Center for Cosmology and Astrophysics, Department of Physics, Carnegie Mellon University, 5000 Forbes Avenue, Pittsburgh, PA 15213, USA*
[18]*Astrophysics Research Institute, Liverpool John Moores University, 146 Brownlow Hill, Liverpool L3 5RF, UK*
[19]*Department of Astronomy, Cornell University, Ithaca, NY 14853, USA*
[20]*California Institute of Technology, TAPIR, Mail Code 350-17, Pasadena, CA 91125, USA*

[21]*Division of Physics, Mathematics and Astronomy, California Institute of Technology, 1200 E. California Blvd, Pasadena, CA 91125, USA*
[22]*Anton Pannekoek Institute for Astronomy, University of Amsterdam, Science Park 904, NL-1098XH Amsterdam, the Netherlands*
[23]*Department of Physics and Astronomy, University of California, Los Angeles, CA 90095, USA*
[24]*The Oskar Klein Centre, Department of Astronomy, Stockholm University, AlbaNova, SE-10691, Stockholm, Sweden*
[25]*Kavli Institute for Particle Astrophysics and Cosmology, Stanford, CA 94305, USA*
[26]*School of Physics and Astronomy, University of Minnesota, Minneapolis, Minnesota 55455, USA*
[27]*Cahill Center for Astrophysics, California Institute of Technology, MC 249-17, 1200 E California Boulevard, Pasadena, CA 91125, USA*
[28]*IPAC, California Institute of Technology, 1200 E. California Blvd, Pasadena, CA 91125, USA*
[29]*Center for Data Driven Discovery, California Institute of Technology, Pasadena, CA 91125, USA*
[30]*Caltech Optical Observatories, California Institute of Technology, Pasadena, CA 91125, USA*

This paper has been typeset from a TEX/LATEX file prepared by the author.